Constraining a North Atlantic Ocean General Circulation Model with Chlorofluorocarbon Observations

S. L. GRAY

Department of Meteorology, University of Reading, Reading, United Kingdom

T. W. N. HAINE*

Department of Earth and Planetary Sciences, The Johns Hopkins University, Baltimore, Maryland

(Manuscript received 23 July 1999, in final form 26 June 2000)

ABSTRACT

Measurements of anthropogenic tracers such as chlorofluorocarbons and tritium must be quantitatively combined with ocean general circulation models as a component of systematic model development. The authors have developed and tested an inverse method, using a Green's function, to constrain general circulation models with transient tracer data. Using this method chlorofluorocarbon-11 and -12 (CFC-11 and -12) observations are combined with a North Atlantic configuration of the Miami Isopycnic Coordinate Ocean Model with $\frac{1}{3}^\circ$ resolution.

Systematic differences can be seen between the observed CFC concentrations and prior CFC fields simulated by the model. These differences are reduced by the inversion, which determines the optimal gas transfer across the air–sea interface, accounting for uncertainties in the tracer observations. After including the effects of unresolved variability in the CFC fields, the model is found to be inconsistent with the observations because the model/data misfit slightly exceeds the error estimates. By excluding observations in waters ventilated north of the Greenland–Scotland ridge ($\sigma_0 < 27.82$ kg m^{-3}; shallower than about 2000 m), the fit is improved, indicating that the Nordic overflows are poorly represented in the model. Some systematic differences in the model/data residuals remain and are related, in part, to excessively deep model ventilation near Rockall and deficient ventilation in the main thermocline of the eastern subtropical gyre. Nevertheless, there do not appear to be gross errors in the basin-scale model circulation. Analysis of the CFC inventory using the constrained model suggests that the North Atlantic Ocean shallower than about 2000 m was near 20% saturated in the mid-1990s. Overall, this basin is a sink to 22% of the total atmosphere-to-ocean CFC-11 flux—twice the global average value. The average water mass formation rates over the CFC transient are 7.0 and 6.0 Sv (Sv $\equiv 10^6$ m^3 s^{-1}) for subtropical mode water and subpolar mode water, respectively.

1. Introduction

Sophisticated numerical models of the ocean general circulation are playing an increasingly important role in our studies of ocean circulation and processes. As these models become more realistic they must be refined by comparing model fields with observations. Anthropogenic transient tracers such as chlorofluorocarbons (CFCs) and tritium play an important role in this regard. These passive, inert substances have well-known tropospheric concentrations, which vary strongly on decadal timescales. This makes them ideal tracers of the circulation that ventilates the basin-scale ocean. Substantial efforts have been made to obtain high quality datasets from the global ocean over the past two decades [most recently as part of the World Ocean Circulation Experiment (WOCE)]. Many studies aimed at interpreting these measurements have relied on restrictive assumptions about the steadiness and spatial variability of the flow (Jenkins 1988; Pickart et al. 1989; Rhein 1994; Sarmiento 1983). In contrast, the attempts to systematically combine these observations with general circulation models (GCMs) in order to improve the understanding of the ocean circulation are relatively few and recent. England and Maier-Reimer (1999, manuscript submitted to *Rev. Geophys.*) provide a comprehensive review.

The general interpretation of passive tracer distributions in terms of ocean circulation is a problem with many close relatives in geophysics. The quantity of interest (the large-scale, low-frequency flow) cannot be

*Additional affiliation: Atmospheric, Oceanic and Planetary Physics, Department of Physics, University of Oxford, Oxford, United Kingdom.

Corresponding author address: Dr. Suzanne L. Gray, Department of Meteorology, University of Reading, Earley Gate, Reading RG6 6BB, United Kingdom.
E-mail: s.l.gray@rdg.ac.uk

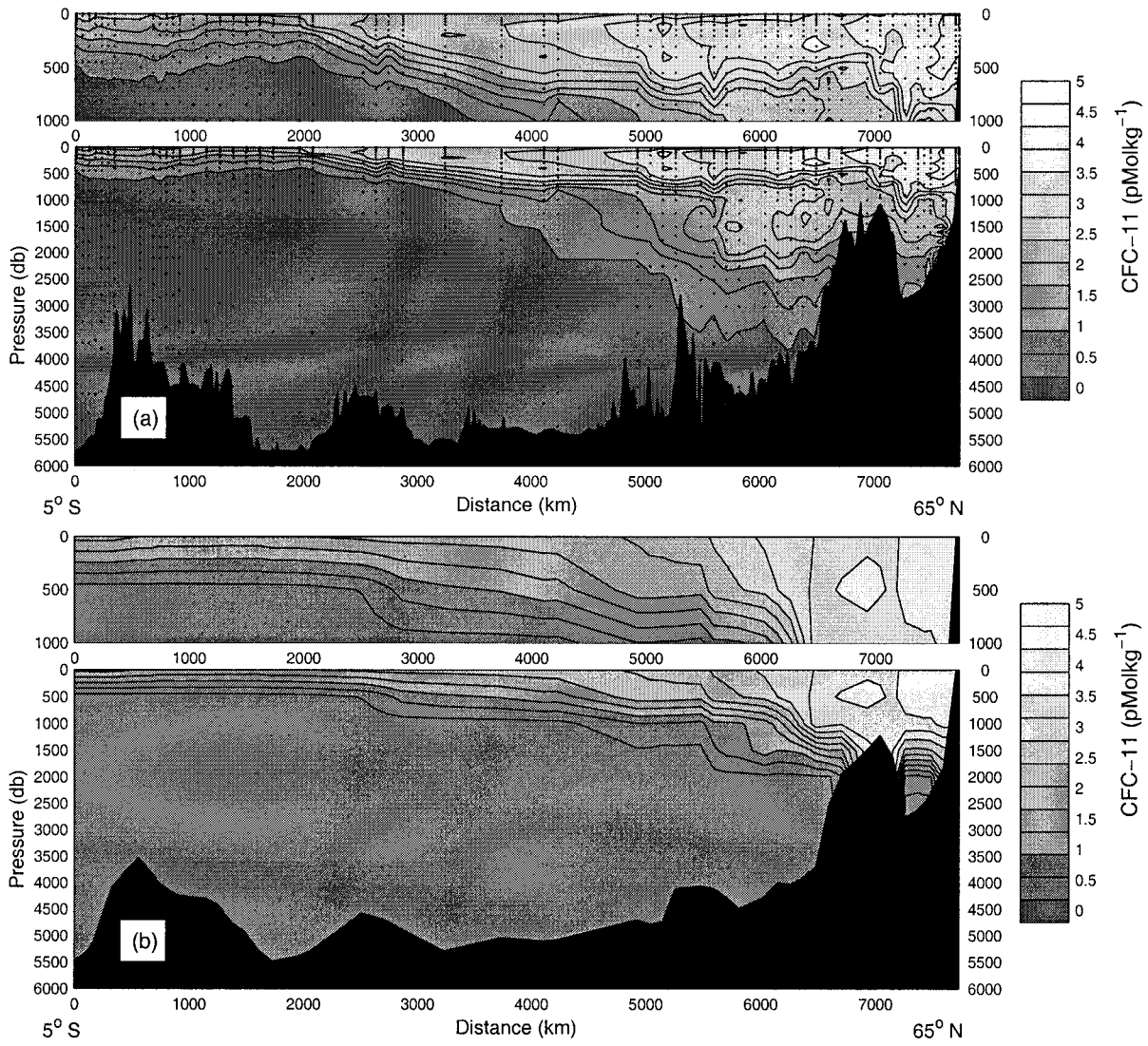

FIG. 1. Section nominally along 20°W of (a) observed (cruise *Malcolm Baldrige* 93-13 1993) and (b) simulated CFC-11 in 1993. Small dots indicate the positions of observations.

directly measured but is related to observations of tracer carried by the flow. An inverse method can be used to indirectly derive information about the flow using predictions of the tracer distribution from a GCM. The methodology used here is to assume that the GCM is perfect and then to determine how reasonable that assumption is. An inverse method is used to determine the best-fit, or optimal, boundary flux of tracer across the air–sea interface, and hence the optimal GCM tracer field. This requires estimates of the uncertainty in the observations and in the tracer boundary flux. A consistency hypothesis that the best-fit predicted tracer fields are statistically consistent with the observations (and hence the model circulation is good) is then tested. If systematic differences exist between observed concentrations and the optimal prediction of these concentrations (i.e., the fit is poor) then the circulation is statistically inconsistent with the observations, and the model circulation requires refinement; the consistency hypothesis must be retested. If, however, the tracer predictions are consistent with the observations, then the data provide no useful additional information about the circulation and it can be concluded that more observations are required. In a certain formal sense it is only possible to learn something new about the circulation if the hypothesis is rejected. The model circulation cannot be ''validated'' or ''verified,'' only shown to be wrong (Wunsch 1996; Oreskes et al. 1994; Randall and Wielicki 1997).

To illustrate these ideas North Atlantic sections of observed and synthetic (model simulated) CFC-11 concentration, nominally along 20°W in 1993, are shown in Fig. 1. Even if the model circulation was perfect, differences in the two tracer fields would arise due to

the errors in the surface CFC fluxes in the model simulation and to errors in the observations. Indeed, Dixon et al. (1996) specifically identify the uncertainty in the air–sea gas flux as the main limit on the quantitative assessment of ocean GCMs using CFCs. Additionally, the ocean model is unable to resolve mesoscale eddies, and so much of the fine-scale structure present in the observations cannot be resolved. The question we address here is, given these sources of error, are the synthetic and observed tracer fields statistically different; or, equivalently, is the model circulation consistent with the observations?

Our approach is to generalize and extend the work of Meméry and Wunsch (1990) by developing an inverse method to test the consistency of GCMs with observations of transient tracers. The inverse method is based on Green's functions and has been implemented using a GCM in the North Atlantic Ocean, namely a configuration of the Miami Isopycnic Coordinate Ocean Model (MICOM) with $\frac{4}{3}^\circ$ resolution. A substantial quantity of North Atlantic CFC-11 and CFC-12 data has been collated from hydrographic datasets to test the model. Air–sea CFC fluxes, CFC inventories, residence times, and water mass formation rates for the North Atlantic constrained by these observations are also shown and discussed. The paper is organized as follows: Section 2 describes the Green's function theory used to solve the tracer advection–diffusion equation. The inverse problem, simplifying assumptions and a practical method of calculating the Green's function for a GCM (with associated error in the Green's function method itself) are described in section 3. In section 4 the observational data used and methods of processing are detailed. A brief explanation of the model and the configuration used is given in section 5. Details of the model simulations and results, together with the estimates of the data and tracer boundary flux variances and prior estimates of the flux, are given in section 6. Finally, discussions of the limitations of our method, with their implications, and of the interpretation of these results, and the conclusions are reported in sections 7, 8, and 9, respectively. Readers who are already familiar with the inverse theory used may wish to skip to section 4.

2. Green's function theory for the passive tracer equation

The Green's function method is a general technique for constructing the solution to an inhomogeneous linear differential equation. In physical terms, the field caused by a distributed source is considered as the sum of the effects of each elementary position (these would be equivalent to grid boxes for a numerical model). The Green's function solution to the tracer advection–diffusion equation is discussed in this section.

The advection–diffusion equation for a passive scalar tracer is

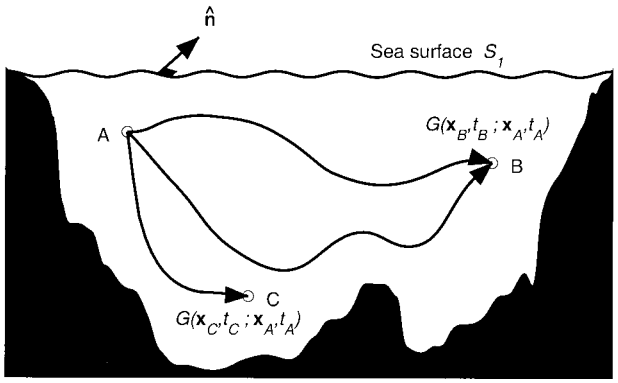

FIG. 2. Schematic of a Green's function component depicting the tracer concentration at the space–time positions *B* and *C*, resulting from a source at the space–time position *A*.

$$\frac{\partial C}{\partial t} + \mathbf{u} \cdot \nabla C - \nabla \cdot (\kappa \nabla C) = q, \tag{1}$$

where the concentration, C, is a function of position $\mathbf{x}$ and time t, $\mathbf{u}(\mathbf{x}, t)$ is the three-dimensional incompressible flow, $\kappa(\mathbf{x}, t)$ is the diffusion coefficient, and $q(\mathbf{x}, t)$ represents (known) interior sources or sinks of the tracer. The fluid is contained in the region R and bounded by the surface S. The initial and boundary conditions are given by

$$\text{ICs:} \quad C(\mathbf{x}, 0) = I(\mathbf{x}) \tag{2}$$

$$\text{BCs:} \quad C(\mathbf{x}_S, t) = B_D(\mathbf{x}_S, t) \quad \text{Dirichlet} \tag{3}$$

and/or

$$\kappa(\mathbf{x}_S, t)\nabla C(\mathbf{x}_S, t) \cdot \mathbf{n} = B_N(\mathbf{x}_S, t) \quad \text{Neumann,} \tag{4}$$

where $\mathbf{x}_S$ is the location of the boundary and $\mathbf{n}$ is the unit normal vector there. Here we have a choice of specifying the value of C on the boundary (Dirichlet conditions) or the flux of tracer through the boundary (Neumann conditions) (the case of specifying a linear combination of Dirichlet and Neumann boundary conditions will not be dealt with here, although we do allow the possibility of specifying Dirichlet conditions for some regions of S and Neumann conditions elsewhere).

To solve this linear parabolic system the associated Green's function is defined (e.g., Morse and Feshbach 1953). The Green's function used is the solution to the inhomogeneous tracer equation with homogeneous boundary conditions and is defined as the solution to

$$\frac{\partial G}{\partial t} + \mathbf{u} \cdot \nabla G - \nabla \cdot (\kappa \nabla G) = \delta(\mathbf{x} - \mathbf{x}_0, t - t_0), \tag{5}$$

where $\delta(\mathbf{x} - \mathbf{x}_0, t - t_0)$ is the Dirac delta function located at position $\mathbf{x}_0$ and time t_0, and the ∇ operator acts over $\mathbf{x}$. In this context, the Green's function $G(\mathbf{x}, t; \mathbf{x}_0, t_0)$ can be regarded as the tracer concentration at $\mathbf{x}$ and t resulting from an impulsive tracer source at $\mathbf{x}_0$ and t_0. This is shown schematically in Fig. 2 as the tracer concentration at the space–time positions *B* and

C resulting from a source at the space–time position A. Equation (5) may be viewed as an equation for G at $(\mathbf{x}, t)$ with parameters $\mathbf{x}_0$ and t_0. Homogeneous boundary conditions apply to this Green's function problem,

$$G(\mathbf{x}_S, t; \mathbf{x}_0, t_0) = 0 \quad \text{Dirichlet}$$

and/or

$$\nabla G(\mathbf{x}_S, t; \mathbf{x}_0, t_0) \cdot \mathbf{n} = 0 \quad \text{Neumann} \tag{6}$$

according to the boundary condition on C.

The Green's function solution to this problem, derived in appendix A, is given by

$$C(\mathbf{x}, t) = \int_0^t \int_R G(\mathbf{x}, t; \mathbf{x}_0, t_0) q(\mathbf{x}_0, t_0)\, dt_0\, dV_0 + \int_R G(\mathbf{x}, t; \mathbf{x}_0, 0) I(\mathbf{x}_0)\, dV_0$$
$$+ \int_0^t \int_S \{G(\mathbf{x}, t; \mathbf{x}_S, t_0) B_N(\mathbf{x}_S, t_0) - \kappa(\mathbf{x}_S, t_0)[\nabla_0 G(\mathbf{x}, t; \mathbf{x}_S, t_0) \cdot \mathbf{n}] B_D(\mathbf{x}_S, t_0)\}\, dS_0\, dt_0. \tag{7}$$

The three terms in (7) arise from the three inhomogeneous contributions to the tracer field. They are readily interpreted as the tracer concentration at $\mathbf{x}$ and t resulting from:

1) the internal source or sink of tracer q
2) the initial tracer present at time $t = 0$, $I(\mathbf{x})$
3) the tracer that enters the domain across the boundary, either by setting C at the boundary itself [$B_D(\mathbf{x}_S, t_0)$, Dirichlet conditions] or its gradient (the tracer flux) [$B_N(\mathbf{x}_S, t_0)$, Neumann conditions].

Note that the representation of the tracer field by integrals of the Green's function with inhomogeneous source terms is entirely general. The Green's function itself is determined by the flow field, diffusion coefficient, and class of boundary conditions on C. It does not depend on the details of either the source q, the initial tracer conditions I, or the boundary conditions B. In this sense, once the Green's function has been found, *any* tracer distribution can be determined by explicitly evaluating (7) for the specific conditions of interest. Indeed, (7) applies for *any* (bounded and nondivergent) circulation or diffusion coefficient, including the explicit molecular diffusivity. These general properties mean that the Green's function has a very wide application for interpreting the flow. In particular, a generalized water mass analysis and fluid age diagnosis may be performed using the Green's function (Hall and Plumb 1994; Holzer and Hall 2000) We postpone a detailed discussion of these issues to another paper. However, a related quantity, the tracer inventory, is calculated in section 8. This approach can be used for any tracer which satisfies a linear evolution equation.

3. The transient tracer inverse problem

The inverse transient tracer problem is stated and then solved using the Green's function in this section. The continuous solution is given first followed by discussion of the discrete, practical implementation. The statement of, and the Green's function solution to, the inverse tracer problem are given in sections 3a and 3b. Important assumptions made to simplify the application of the inverse method are discussed in section 3c. Finally, the implementation of the Green's function inverse calculation is discussed in section 3d.

a. Statement of the inverse problem

We consider an atmospheric transient tracer that is materially conserved in the ocean. We assume that the background concentration of the tracer is zero and that there are no interior sources or sinks [for the case of anthropogenic tritium there is an interior sink due to radioactive decay to helium-3, which could be easily included in the formalism that follows by modifying the governing concentration equation (1) although it cannot be treated as a prescribed sink, q]. Tracer enters the ocean via a flux condition at the sea surface and there is no flux through the seafloor. Using the notation developed in section 2,

$$C(\mathbf{x}, 0) = 0 \tag{8}$$

$$\kappa(\mathbf{x}, t)\nabla C(\mathbf{x}_{S_1}, t) \cdot \mathbf{n} = \begin{cases} B_N(\mathbf{x}_S, t) & \text{on } S = S_1 \quad (9) \\ 0, & \text{elsewhere,} \quad (10) \end{cases}$$

where S_1 is the sea surface. The concentration is given by

$$C(\mathbf{x}, t) = \int_0^t \int_{S_1} G(\mathbf{x}, t; \mathbf{x}_S, t_0) B_N(\mathbf{x}_S, t_0)\, dS\, dt_0 \tag{11}$$

by substituting (9)–(10) into (7).

The first step is to pose the problem as a mathematical hypothesis that can be statistically tested. The a priori knowledge of the circulation is summarized by specifying the flow $\mathbf{u}$ and diffusion coefficient κ. There is also an estimate of the air–sea tracer flux, b_1, such that

$$B_N(\mathbf{x}_{S_1}, t) = b_1(\mathbf{x}_{S_1}, t) + n_b(\mathbf{x}_{S_1}, t), \tag{12}$$

where n_b is the difference between the true value of

the flux and the prior estimate. Typically, the flux is written as

$$b_1(\mathbf{x}_{S_1}, t) = k[F(\mathbf{x}_{S_1}, t)C_{\text{atm}}(t) - C(\mathbf{x}_{S_1}, t)], \quad (13)$$

where k is an air–sea transfer coefficient (a piston velocity that is a poorly known function of wind speed, temperature, and tracer species), F is the tracer solubility (a function of temperature, salinity, and tracer species), and C_{atm} is the atmospheric mixing ratio of the tracer (assumed to be spatially uniform). A feedback between the ocean surface and the atmosphere is implied by (13), so it appears that b_1 cannot be determined independently of the surface tracer concentration $C(\mathbf{x}_{S_1}, t)$. Although this feedback does occur in the forward integration, in the inverse calculation the optimal flux boundary condition is determined independently (as the forward integration is only used to provide prior estimates of the fluxes).

The covariance, C_b, for n_b is

$$C_b(\mathbf{x}, t, \mathbf{x}_0, t_0) = \langle n_b(\mathbf{x}, t)n_b(\mathbf{x}_0, t_0)\rangle \quad \text{for } \mathbf{x}, \mathbf{x}_0 \in \mathbf{x}_{S_1}, \quad (14)$$

where the angle brackets denote the expectation and $\langle n_b\rangle = 0$ is assumed. Finally, there is a set of M observations, $\mathbf{d}$, of tracer in the ocean which satisfy

$$\mathbf{d}(\mathbf{x}_d, t_d) = C(\mathbf{x}_d, t_d) + \mathbf{n}_d(\mathbf{x}_d, t_d), \quad (15)$$

where the boldface denotes $M \times 1$ column vectors at positions $\mathbf{x}_d$ and times t_d. The error, $\mathbf{n}_d$, has zero mean and covariance $\mathbf{C}_d$. These quantities are summarized in Table 1. Next, the null hypothesis, $\mathcal{H}_0$, is defined:

- Hypothesis $\mathcal{H}_0$: The observations, $\mathbf{d}$, are statistically consistent with the circulation defined by $\mathbf{u}$ and κ, the boundary condition defined by b_1, and the covariances $\mathbf{C}_d$ and C_b.

To confirm or reject $\mathcal{H}_0$ the boundary condition that is *most* consistent with the prior information must be found. This is done in the usual way, by determining the minimum value of a quadratic objective scalar functional, $\mathcal{J}$. The next step is to estimate the ''goodness of fit,'' or equivalently the likelihood that this minimum value occurred by chance. The chi-square (χ^2) probability distribution is used to test this and, hence, the hypothesis can be statistically established or refuted.

In this context the objective functional is defined by

$$\mathcal{J} = \mathbf{n}_d^{\mathrm{T}} P_d \mathbf{n}_d + \int_0^{t_f}\int_0^{t_f}\int_{S_1}\int_{S_1} n_b(\mathbf{x}, t)P_b(\mathbf{x}, t, \mathbf{x}_0, t_0)n_b(\mathbf{x}_0, t_0)\, dS\, dS_0\, dt\, dt_0, \quad (16)$$

where t_f is the final time of interest. This form balances the model/data misfit (first term on the right-hand side) and the deviation of the tracer flux from its prior estimate (second term). The weights P_b and $\mathbf{P}_d$ are covariance inverses such that

$$\mathbf{P}_d\mathbf{C}_d = \mathbf{I} \quad (17)$$

and

$$\int\int P_b(\mathbf{x}, t, \mathbf{x}_0, t_0)C_b(\mathbf{x}_0, t_0, \mathbf{x}_1, t_1)\, dS_0\, dt_0 = \delta(\mathbf{x} - \mathbf{x}_1, t - t_1), \quad (18)$$

where $\mathbf{I}$ is the $M \times M$ identity matrix, $\mathbf{x}$ and $\mathbf{x}_0$ both lie on S_1, and we assume that $\mathbf{C}_d$ is sufficiently well behaved that $\mathbf{P}_d$ exists.

b. Solution to the inverse problem

Several approaches exist to determine the minimum of $\mathcal{J}$ (see Wunsch 1996). There are two key steps in any method: first, the relationship between $\mathbf{u}$, κ, and the concentration C must be included in $\mathcal{J}$ and, second, anticipating that this relationship cannot be expressed in closed form, the system must be discretized and solved numerically. Just one route to solve this problem is presented here; $\mathcal{J}$ is minimized using calculus of variations after substituting for C in terms of the Green's function using (11). The problem can then be discretized and the resulting linear system solved directly. The minimum of $\mathcal{J}$ is given by the optimal choice of boundary condition, $\hat{b}$, which is derived, in the continuous form, in appendix B. In a discrete formulation where the continuous fields over space and time are replaced with a finite number of values at fixed points, (B5) becomes

$$\hat{\mathbf{b}} = (\mathbf{G}_d^{\mathrm{T}}\mathbf{P}_d\mathbf{G}_d + \mathbf{P}_b)^{-1}(\mathbf{G}_d^{\mathrm{T}}\mathbf{P}_d\mathbf{d} + \mathbf{P}_b\mathbf{b}_1). \quad (19)$$

If N is the number of discrete locations in space–time on the surface S_1, then $\hat{\mathbf{b}}$ and $\mathbf{b}_1$ are $N \times 1$ vectors, $\mathbf{P}_b$ is an $N \times N$ weight matrix, and $\mathbf{G}_d = \mathbf{G}(\mathbf{x}_d, t_d; \mathbf{x}_0, t_0)$ is an $M \times N$ matrix of components of the Green's function. Note that (19) has the standard form of a tapered, weighted least squares problem (e.g., Wunsch 1996). The strength of the Green's function method is that it casts problems in linear differential equations into simple matrix systems. A powerful method of evaluating (19) numerically is to use singular value decomposition (see, e.g., Press et al. 1992).

The probability distribution for different values of the objective functional, $\mathcal{J}$, at its minimum can be used as a measure of the goodness of fit of the solution to (19),

TABLE 1. Notation.

Variable	Description
R	Domain of interest
S	Bounding surface of domain
S_1	Ocean surface
$\mathbf{u}$	Prior estimate of circulation
κ	Prior estimate of diffusion coefficient
C	Tracer concentration
G	Green's function for tracer equation
$G\dagger$	Adjoint Green's function
G'	Time integrated Green's function
q	Tracer source or sink
Q	Goodness of fit
I	Initial tracer concentration
B_D	Dirichlet (concentration) tracer boundary condition
B_N	Neumann (flux) tracer boundary condition
$\mathbf{d}$	$M \times 1$ column vector of tracer observations
$\mathbf{x}_d$	$M \times 1$ column vector of tracer observation locations
$\mathbf{t}_d$	$M \times 1$ column vector of tracer observation times
$\mathbf{n}_d$	Observation error
$\mathbf{C}_d$	Observation error covariance matrix ($M \times M$)
$\mathbf{P}_d$	Data weight matrix ($M \times M$)
$\hat{b}$	Optimal estimate of air/sea tracer flux
b_1	Prior estimate of air/sea tracer flux
n_b	Error in air/sea tracer flux
C_b	Air/sea tracer flux error covariance function
P_b	Air/sea tracer flux weight function
k	Piston velocity or air/sea transfer coefficient
F	Solubility function
C_{atm}	Atmospheric mixing ratio of tracer species
M	Number of tracer observations
N	Number of boundary points in space and time
$\circ$	Integration over S and time
ξ	Mixed layer tracer saturation
$\mathcal{J}$	Objective functional (or cost function)
I_v	Inventory

or equivalently as a measure of the validity of the null hypothesis, $\mathcal{H}_0$. This is the χ^2 distribution function for $\nu = M - N$ degrees of freedom. The goodness of fit is given by $Q = 1 - P(\mathcal{J}, \nu)$, which is the probability that the objective functional will exceed a particular value of $\mathcal{J}$ by chance given ν degrees of freedom. If Q is very small, then the apparent discrepancies between the observed data and the model predictions are unlikely to be chance fluctuations. Additional constraints, such as correlations between observations, will act to reduce the number of degrees of freedom available (similarly correlations between elements of the flux boundary condition will act to increase the number of degrees of freedom).

The posterior (constrained by the inverse calculation) residuals for the data and flux boundary condition are given by $(\mathbf{G}_d\hat{\mathbf{b}} - \mathbf{d})$ and $(\hat{\mathbf{b}} - \mathbf{b}_1)$, respectively. These must be statistically independent if the null hypothesis is to be accepted, even if Q is large ($\approx$1). Random fractional residuals (i.e., residuals scaled by the square root of the leading diagonals of the covariances $\mathbf{C}_d$ and $\mathbf{C}_b$) should have a Gaussian distribution with zero bias and a standard deviation of 1.

Finally, the difference between the prior and posterior objective functional indicates the degree to which the data has constrained the inverse model. The prior objective functional is given in discrete form by $\mathcal{J}_d[\mathbf{b}_1] = (\mathbf{d} - \mathbf{G}_d\mathbf{b}_1)^{\mathrm{T}}\mathbf{P}_d(\mathbf{d} - \mathbf{G}_d\mathbf{b}_1)$. The posterior objective functional can be decomposed into two components, $\mathcal{J}_d$ and $\mathcal{J}_b$, where $\mathcal{J}_d[\hat{\mathbf{b}}] = (\mathbf{d} - \mathbf{G}_d\hat{\mathbf{b}})^{\mathrm{T}}\mathbf{P}_d(\mathbf{d} - \mathbf{G}_d\hat{\mathbf{b}})$ is due to the misfit between the observed and fitted data and $\mathcal{J}_b[\hat{\mathbf{b}}] = (\hat{\mathbf{b}} - \mathbf{b}_1)^{\mathrm{T}}\mathbf{P}_b(\hat{\mathbf{b}} - \mathbf{b}_1)$ is due to the misfit between prior estimates of and fitted values for the boundary conditions.

c. Simplifying assumptions

The inverse calculation is simplified in practice as follows.

1) THE STEADY FLOW ASSUMPTION

If the flow and diffusivity are both constant in time then the Green's function satisfies a *translation* principle:

$$G(\mathbf{x}, t; \mathbf{x}_0, t_0) = G(\mathbf{x}, t - t_0; \mathbf{x}_0, 0). \qquad (20)$$

Only the elapsed time, $t - t_0$, after the impulsive tracer source is important and not the absolute times of the impulse and observation. This reduces the computational expense of the calculation. It implies that an impulsive tracer source, measured frequently (e.g., at t_1, t_2, and t_3) until the observation time t, can be used to represent the tracer distribution at the observation time from impulsive tracer sources injected at all times prior to this (at $t - t_1$, $t - t_2$, and $t - t_3$).

2) SEPARABLE BOUNDARY CONDITIONS

The tracer boundary condition is split into separate spatially and temporally varying components. To do this we assume that the saturation in the mixed layer [$\xi = C(\mathbf{x}_{S_1}, t)/(FC_{\mathrm{atm}}(t))$] is constant at a given point on interannual timescales (Haine and Richards 1995; Haine and Gray 2000). The boundary condition, given by the tracer flux equation (13), can then be rewritten as $b_1 = kFC_{\mathrm{atm}}(1 - \xi)$, where the solubility F, the piston velocity k, and the saturation ξ are independent of time on interannual timescales. The atmospheric tracer concentration C_{atm} is spatially uniform with a well-known temporal component, $f(t)$. Separating the tracer flux in this way greatly simplifies the inversion by reducing it from an estimation problem for the boundary condition as a function of space and time to one in space only. Consequently, (19) can be expressed as a function of space only by using a modified Green's function given by

$$\mathbf{G}'(\mathbf{x}_d, \mathbf{x}_0) = \sum_{t_0=0}^{\mathbf{t}_d} \mathbf{G}_d(\mathbf{x}_d, \mathbf{t}_d - t_0; \mathbf{x}_0, 0) f(t_0)\Delta t, \qquad (21)$$

where $\mathbf{t}_d$ is the vector of observation times corresponding to measurements at locations $\mathbf{x}_d$, and Δt is the time interval between realizations of $\mathbf{G}_d$. Using the steady

flow assumption, the time-integrated Green's function $\mathbf{G}'$ depends only on the elapsed time between the observations and the various tracer impulses.

d. Implementation of the inverse calculation

The method of calculating the Green's function and errors in the method itself are explained here.

1) CALCULATION OF THE TRACER GREEN'S FUNCTION

The function $G(\mathbf{x}, t; \mathbf{x}_0, t_0)$ is the tracer distribution at all points and all times due to impulse tracer sources at all points and all times. In a gridpoint model this continuous function is discretized and, in principle, the fields from impulsive sources at each grid point at every time step are required. An alternative is to use smooth, smeared sources of tracer concentration instead of delta functions (with an integrated amplitude normalized to unity). These are computationally stable (no sharp gradients) and represent a region of the ocean surface rather than a single grid point, so fewer are required. The size and shape of these smeared sources are chosen to give the highest resolution in the main ventilation regions. The number of Green's function components required reflects the distinct pathways for tracer transport into the ocean interior and is thus related to the number of distinct water masses formed. The Green's function components are stored annually, consistent with the assumptions of steady flow and boundary condition separability, both of which are only valid when considering interannual timescales. Late summer (the end of August) was chosen as the storage time for two reasons: first, the majority of the observational data available (particularly from the northern part of the domain) was collected in the summer months and, second, this is the season when the interior tracer fields are likely to be least sensitive to the details of the deep convection, which occurs in the winter months.

2) ESTIMATION OF THE METHOD ERROR

The assumptions that make the inverse calculation tractable have the countereffect of introducing an error associated with the Green's function method itself. This method error is in addition to the data and flux errors that are accounted for by the weights $\mathbf{P}_d$ and $\mathbf{P}_b$. It is also distinct from the model error arising from inconsistencies between the model, observations, and the prior estimates of the boundary condition.

Clearly, an estimate of this method error is essential. To isolate the method error from the model error an inverse calculation is performed for a case where the model is perfect. This is achieved by using synthetic CFC-11 and CFC-12 observations generated by integrations of the GCM in question. Errors due to the Green's function method are solely responsible for any misfit between the model, synthetic data, and the prior estimates of the boundary flux (also determined from the model). The method error is determined by performing the inverse calculation using prescribed uncertainties consistent with random error added to the data and flux vectors. These uncertainties are adjusted until the null hypothesis is just satisfied. For the inverse method to be useful, they must be smaller than the real errors estimated in the observations and prior flux. The method error is sensitive to the number, positions, and years of the observations. Hence, when performing the inverse calculation with synthetic data, the real observation positions and times are used.

3) USE OF MORE THAN ONE TRACER SPECIES

The use of two or more tracer species, which have different source functions, flux properties, and data locations, increases the constraints on the model circulation. A separate inverse calculation could be performed for each tracer species. However, a combined inversion has the advantage that a single measure of the goodness of fit of the model with the data and prior estimates is obtained. For more than one tracer species the discrete Green's function, $\mathbf{G}_d$, is written in the form

$$\mathbf{G}_d = \begin{bmatrix} {}^1\mathbf{G}_d & 0 & 0 \\ 0 & {}^2\mathbf{G}_d & 0 \\ & & \ddots \\ 0 & 0 & {}^{sp}\mathbf{G}_d \end{bmatrix}, \tag{22}$$

where the superscripts $i = 1, 2, \cdots, sp$ denote different tracer species. The data, $\mathbf{d}$, and predicted flux, $\hat{\mathbf{b}}$, vectors are extended in a corresponding manner.

4. North Atlantic chlorofluorocarbon observations

a. Data sources

A substantial quantity of pre-WOCE and WOCE CFC-11 and CFC-12 data in the North Atlantic has been collated (over 15 000 measurements of both CFC-11 and -12 are used). The cruises span the years 1982–1994 and cover most regions in the North Atlantic during that period (Fig. 3). Table 2 lists the cruise names and cites references for each dataset. (We gratefully acknowledge the assistance and advice given by the investigators who provided these measurements for our analysis.) The locations of observations are slightly different for each tracer species since measurements for both were not obtained from all bottles. Where available, data flags were used to eliminate bad CFC measurements and water samples for which the potential density, σ_0, could not be calculated.

b. Data processing

The CFC data is binned meridionally, zonally, and vertically (in model density layers; see section 5). If a

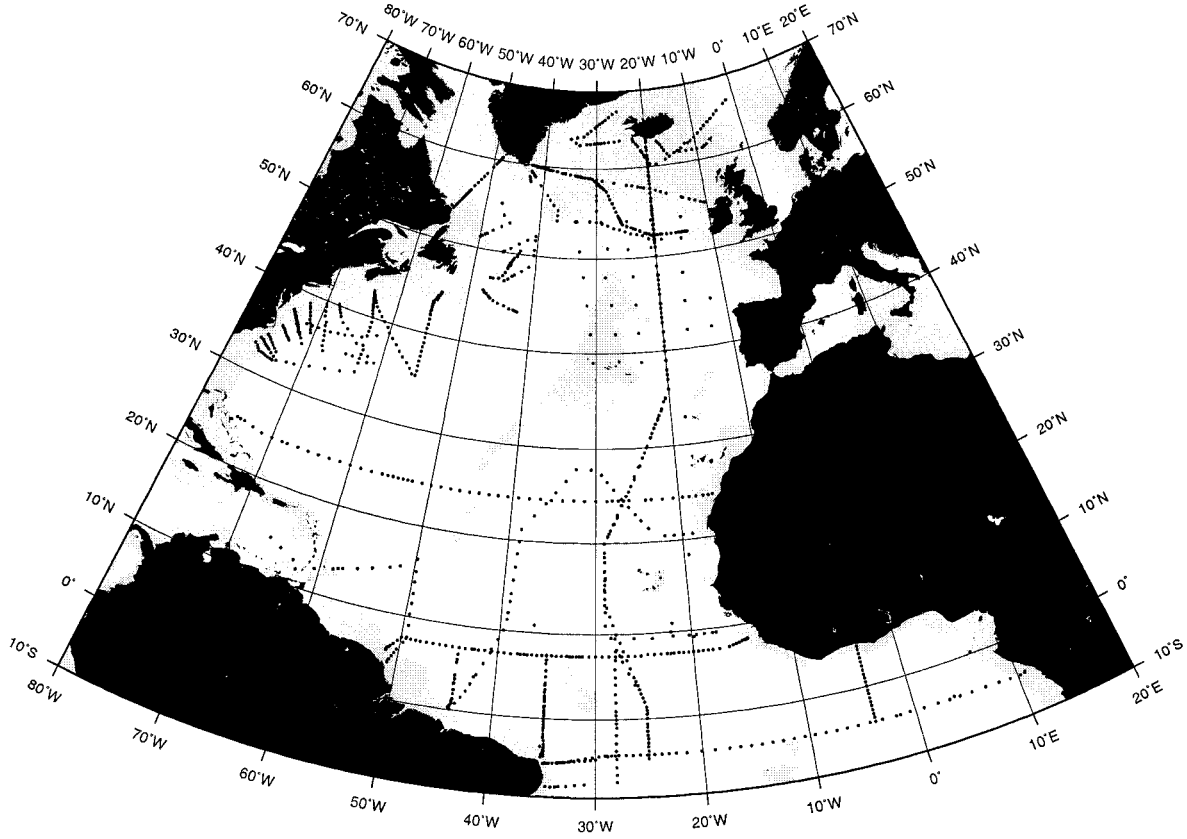

FIG. 3. Positions of CFC-11 and/or -12 stations used (1982–94; see Table 2). The shading shows ocean regions shallower than 3000 m.

TABLE 2. Chlorofluorocarbon data sources.

Cruise	Season	Year*	Reference
Transient tracers in the ocean: Tropical Atlantic Study (TTO–TAS) Oceanus134	Winter	1982	Weiss et al. (1991)
	Summer	1983	Hogg et al. (1986) Pickart et al. (1989) Smethie (1993)
Knorr134 part of WBEX (Western Boundary Exchange Experiment)	Summer	1986	Smethie (1993)
Oceanus202	Summer	1988	Doney and Bullister (1992)
Endeavor214	Summer	1990	Pickart and Smethie (1993) Pickart et al. (1992)
Endeavor223	Winter	1990	Pickart et al. (1996) McKee et al. (1995)
WOCE section ar04a	Winter	1990	WOCE Data Products Committee (1998)
WOCE section ar04b	Summer	1991	WOCE Data Products Committee (1998)
WOCE section a01e	Summer	1991	WOCE Data Products Committee (1998)
Charles Darwin 62 (CONVEX)	Summer	1991	D. Smythe-Wright (1998, personal communcation)
Charles Darwin 58 and 59 (VIVALDI 91)	Summer	1991	Griffths et al. (1992)
WOCE section ar04c	Winter	1992	WOCE Data Products Committee (1998)
WOCE section ar07wc	Summer	1992	WOCE Data Products Committee (1998)
WOCE section a05	Summer	1992	WOCE Data Products Committee (1998)
Johan Hjort (section ar18)	Summer	1994	E. Fogelqvist (1998, personal communication)
Circulation Thermohaline 1 (CITHER1)	Winter	1992	Andrié et al. (1998)
WOCE section ar07wd	Summer	1993	WOCE Data Products Committee (1998)
Malcolm Baldrige 93–13 (N.Atl-93)	Summer	1993	Castle et al. (1997) Doney et al. (1998)
Section a01ew	Winter	1994	M. Rhein (1998, personal communication)

* Year is that of the previous summer if winter data.

datum has a potential density less than that of the mixed layer, then it is binned into the mixed layer; otherwise, the datum is binned into the model layer having the closest value of σ_0 (ignoring layers that have zero thickness in that column). Box averages are calculated where more than one observation was present in a grid box in a given year.

Since the numerical Green's function is stored annually at the end of August, the observations must be adjusted to late summer values. The data are processed according to a simple paradigm of permanent tracer subduction during late winter/early spring (around March) as the mixed layer rapidly shallows after the deep convection of the winter months (Haine and Richards 1995). It continues to shallow during the summer, reaching its minimum depth around September. At this time tracer concentrations in the ocean interior vary slowly through advection and diffusion.

Tracer observations made between March and September are assumed to be valid in late summer of that year. The potential densities of the model layers in September are used to define the mixed layer and perform the vertical data binning. It is implicitly assumed that the gentle shoaling of the mixed layer during the summer months has little effect on the observations. In contrast, observations made between September and March are assumed to be valid for the previous summer, and the March model layer potential densities are used. Data in the model mixed layer are not used due to the sensitivity of CFC concentrations to localized, rapid mixing events such as convection.

5. Ocean general circulation model

The ocean general circulation model used in this paper is a North Atlantic implementation of the Miami Isopycnic Coordinate Ocean Model (MICOM, version 2.6: Bleck et al. 1992). This GCM uses potential density as the vertical coordinate, which is advantageous for our purposes since tracers mix preferentially along isopycnals. The Atlantic version of this model has a reasonably realistic circulation capturing the primary ventilation pathways (New et al. 1995). This model has also been used by Jia and Richards (1996) to simulate tritium and helium-3. These authors found good agreement with observations, concluding that the major circulations and the sequestration of transient tracers into the ocean interior are well represented in the model. They did not, however, use the quantitative inverse approach developed in this paper.

a. Brief description of the model

MICOM is a primitive equation numerical ocean model that simulates the evolution of momentum, mass, heat, and salt in the ocean. It has been documented in a collection of papers by Bleck and coworkers (in particular, Bleck et al. 1992, 1989; Bleck and Smith 1990). The configuration of the model used in this study is a coarse-resolution version of that used in the DYNAMO (Dynamics of North Atlantic Models) intercomparison project (The DYNAMO Group 1997). Recent work by Jia (2000) also used the model in this configuration. Only basic aspects of the configuration are repeated here.

The resolution is $\frac{1}{3}^\circ$ in longitude and $\frac{1}{3}^\circ$ cos(lat) in latitude, yielding an isotropic grid. The domain extends from approximately 20°S to 70°N, 100°E to 20°W with closed model boundaries and sponge layers to the north and south, and associated with the Strait of Gibraltar. The northern sponge layer extends north of 67°N, between 40° and 10°W, and north of the line joining 67°N, 10°W, and 60°N, 17.5°E (where 17.5°E is the eastern boundary of the model). The southern sponge layer extends south of 11.5°S. Pressure (below the mixed layer) and salinity are relaxed to climatological values across these layers (on a timescale that decreases towards the outer edges of the sponge layers). There are 20 layers in the vertical, the uppermost of which is a mixed layer that uses the Kraus–Turner mixed layer parameterization (Kraus and Turner 1967). This layer is homogeneous in the vertical but varies in density, depth, and other properties in the horizontal. The layers below the mixed layer have constant potential density (σ_0, referenced to the surface, zero pressure). The model is forced with monthly climatological surface forcing fields derived from the ECMWF analysis (1986–88), with the sea surface salinity relaxing to the Levitus (1982) climatology. Subgrid-scale processes are parameterized using Laplacian diffusion. The mixing coefficients are defined in terms of diffusion velocities (the ratio of the diffusion coefficient to the grid size) and have the magnitudes 0.5, 0.5, and 1.0 cm s^{-1} for thickness, tracers (including temperature and salinity), and momentum, respectively. This configuration includes a small amount of diapycnal mixing, the magnitude of which is related to the buoyancy frequency and thus is greatest in the upper regions of the ocean where large vertical gradients in temperature and salinity exist. The product of the diapycnal diffusivity and the buoyancy frequency is 10^{-7} m^2 s^{-2}. The simulations performed here were initiated with equilibrated model fields obtained from a model simulation that had been integrated for over 30 years and had reached an approximately steady state on interannual timescales.

b. The tracer model

A model for transient tracers was incorporated into the Atlantic isopycnic model. The advective and diffusive behavior of the tracer is identical to that of salinity. The model Green's function is calculated by treating each component as an independent tracer.

Across the sponge layers at the northern and southern boundaries the tracer concentrations are relaxed to zero (on the same timescales as the dynamical variables).

This is the appropriate boundary condition for the Green's function since an initial condition of zero tracer concentration and homogeneous boundary conditions apply. These boundary conditions are also used when generating the synthetic tracer data despite the probable transfer of some tracer across the northern and southern boundaries in the real ocean. These neglected lateral boundary sources of CFCs could be represented by additional components of the model Green's function calculated from impulse sources just inside the vertical walls. However, it would be difficult to obtain associated prior flux estimates as this would require knowledge of the tracer flux across these lateral boundaries (other neglected sources such as river runoff and precipitation could also be represented in this way). The initial condition for the Green's function consists of isolated tracer patches in the mixed layer (section 6b). There is no flux of tracer across the ocean–atmosphere interface in these calculations. A negligible (zero) background tracer concentration is used to generate the synthetic data.

The solubilities of the CFCs in seawater are calculated according to the formulas given by Warner and Weiss (1985). The piston velocity k is parameterized in terms of the wind speed referenced to 10-m height and the Schmidt number (the ratio of the kinematic viscosity to the molecular diffusivity of the solute). Two common parameterizations are a three-segment, piecewise linear relation (Liss and Merlivat 1986) and a quadratic relation (Wanninkhof 1992). The 10-m wind speeds used in the tracer model for calculation of the piston velocities are taken from the da Silva et al. (1994) climatology, and the Schmidt number is calculated according to the formulas given in Wanninkhof (1992). On the basis of comparison with field data, it is not possible to determine which of the two parameterizations is preferable (Asher and Wanninkhof 1998a), and so synthetic data for both tracer species is generated using both parameterizations.

6. Model simulations and results

The model integrations are described in this section. The MICOM tracer Green's function, the error weights, $\mathbf{P}_d$ and $\mathbf{P}_b$, and the prior estimate of the surface CFC flux, $\mathbf{b}_1$, are estimated. The results of the inverse calculations are then given.

A simulation period of 32 years is used beginning from a background state of zero tracer concentration in September 1962. CFCs-11 and -12 were first manufactured in the 1930s and 1940s, and, until the mid-1990s, atmospheric concentrations increased rapidly (Fig. 4). More recently, the rate of increase in the concentrations has slowed markedly (or even reversed) as restrictions on the atmospheric release of these compounds have begun to take effect (Elkins et al. 1993). The tracer concentrations in old water masses (unventilated for several decades) are negligible in comparison with the concentrations in young water masses. Hence the errors introduced by beginning the integration in 1962, rather than earlier, are small.

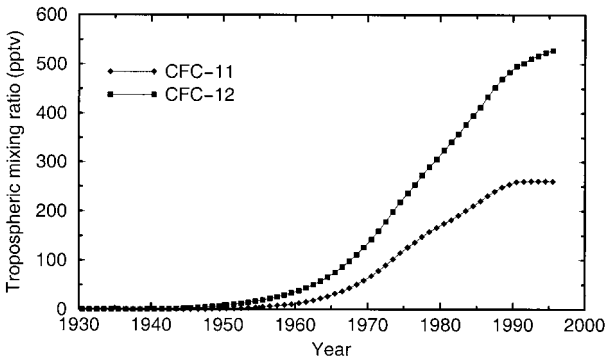

FIG. 4. Northern Hemisphere tropospheric mole fractions of CFC-11 and -12 as functions of time [parts per trillion (pptv) (10^{12})] (Walker et al. 2000).

a. Synthetic CFC observations

Comparison of the synthetic CFC observations (generated using MICOM) with real observations gives a qualitative impression of the accuracy of the model circulation. Synthetic and real CFC-11 observations are contrasted along two sections in Figs. 1 and 5. The first section is nominally along 20°W in 1993, and generally good agreement is seen between the real and synthetic concentrations, although the front at concentrations near 2 pmol kg^{-1} between 5000 and 7000 km is too tight in the model simulation. The second section, nominally along 55°N in 1992, also shows some disparity. In particular, the synthetic CFC-11 concentrations are too high near the surface and too low at depth, and the western boundary currents are not well resolved in the model. Overflows (such as the Denmark Strait overflow) are not well represented in the MICOM circulation. This is in common with other GCMs at this resolution and at eddy-permitting resolution (The DYNAMO Group 1997). The inverse calculation provides a quantitative measure of such inadequacies in the model circulation.

b. The model Green's function

Twenty-three smeared impulse tracer sources are used to estimate the MICOM Green's function. Each source has a two-dimensional Gaussian amplitude function in tracer concentration of the form

$$\exp\left\{-\left[\frac{(i^2+j^2)\{\cos[\arctan(j/i-\theta)]\}^2}{\sigma_i^2} + \frac{(i^2+j^2)\{\sin[\arctan(j/i-\theta)]\}^2}{\sigma_j^2}\right]\right\},$$

where i and j are the number of grid points from the center of the amplitude function in the southern and

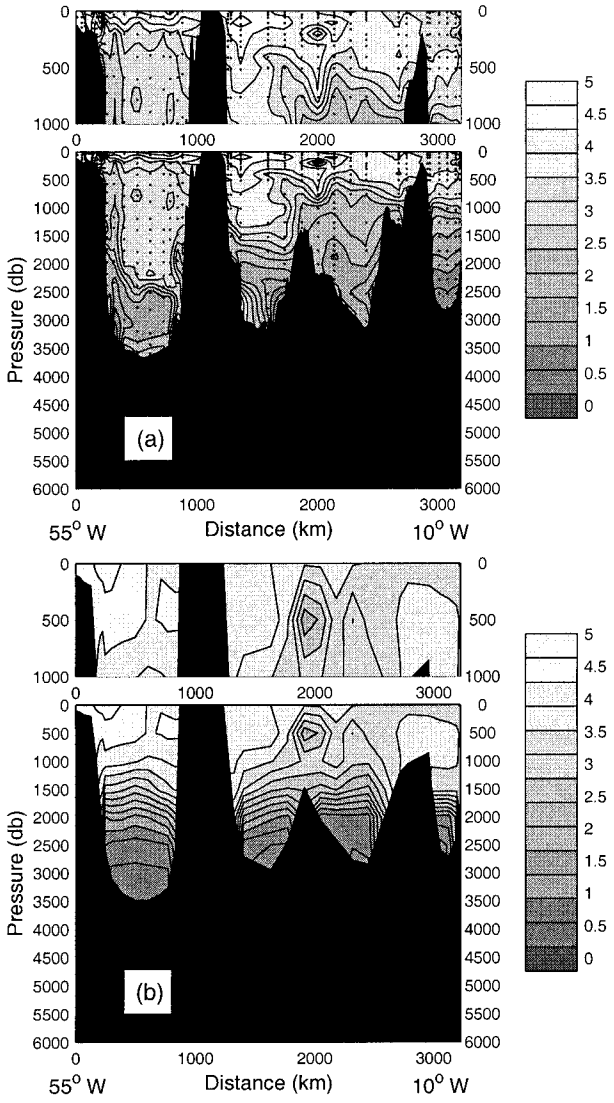

FIG. 5. CFC-11 section nominally along 55°N of (a) observed (cruise *Charles Darwin* 62: CONVEX Experiment, 1991; WOCE section *ar07wd*, 1993) and (b) simulated (1992) CFC-11. Small dots indicate the positions of observations. CFC-11 grayscale units in pmol kg^{-1}.

eastern directions, respectively, σ_i and σ_j are the widths in the north–south and east–west directions, and θ is the angle through which the Gaussian function is rotated in an anticlockwise direction. The amplitude function is normalized to give an integrated total of unity. Of the 23 sources, 13 equally sized circular (in gridpoint space, $\sigma_i = \sigma_j$) sources were spaced evenly over the model domain. The remaining 10 elliptical sources provide additional resolution in regions of high ventilation (Fig. 6). Their positions are based on annual-mean surface fluxes calculated [using (13)] from annual-mean saturations in a preliminary simulation with a simplified flux boundary condition. An advantage of the Green's function method is that these calculations can be iteratively refined by adding additional Green's function components where required. The spread of a single component of the Green's function (impulse source function in the northeastern Atlantic) in a section along 20°W is shown in Fig. 7. Most of the tracer in this component is rapidly subducted into the interior, and the southward spread of the tracer is evident.

c. Estimates of surface CFC flux and the data and flux weights

1) ESTIMATES OF THE SURFACE CFC FLUX

The prior estimates of the flux boundary condition are calculated from the fluxes that occur in the simulations which generate the synthetic CFC observations. A convenient way to represent the response of the surface waters to these fluxes is to consider surface saturation data. The annual-mean saturation as a function of time at three locations is shown in Fig. 8, for CFC-11 using the Wanninkhof (1992) piston velocity parameterization. After an initial rapid increase in the saturation during the first ~2 years of the simulation, a consequence of initiating the model with no tracer in the interior, a gradual increase is observed during the remainder of the simulation. As expected, these changes are anticorrelated with changes in the surface tracer fluxes [not shown; see section 6c(2)].

It is assumed that the saturations of CFCs in the ocean mixed layer can be considered approximately independent of time over long timescales; see section 3c(2). If the flux of tracer into the ocean is a fast process compared to the rate of subduction of tracer into the interior [as indicated by the near-equilibrium saturations often observed (Haine and Richards 1995)], then the surface saturation is constant with time for a tracer with an exponential increase in atmospheric concentration. Figure 8 suggests that the validity of this approximation for CFCs may be region dependent. This is a source of method error as defined in section 3d(2). The gradual increase in surface saturations observed in the model is a response to the slowing in the rate of increase in the atmospheric tracer concentrations with time (from an approximately exponential increase initially to a more linear increase). The differences between the curves for different regions reflect that deeper mixed layers approach equilibrium more slowly (Haine and Richards 1995).

The spatial component of the surface CFC flux is estimated by fitting the model flux to $A(\mathbf{x}_S)C_{\text{atm}}(t)$, where A is the spatial component and $C_{\text{atm}}(t)$ is the temporal component. This is preferable to using a time mean of the flux normalized by the atmospheric concentrations since the fit is weighted more evenly over the period of the simulation. Four fields of spatial flux components are calculated, one for each piston velocity parameterization (Liss and Merlivat 1986; Wanninkhof 1992) and one for each tracer species (CFC-11 and CFC-12). The

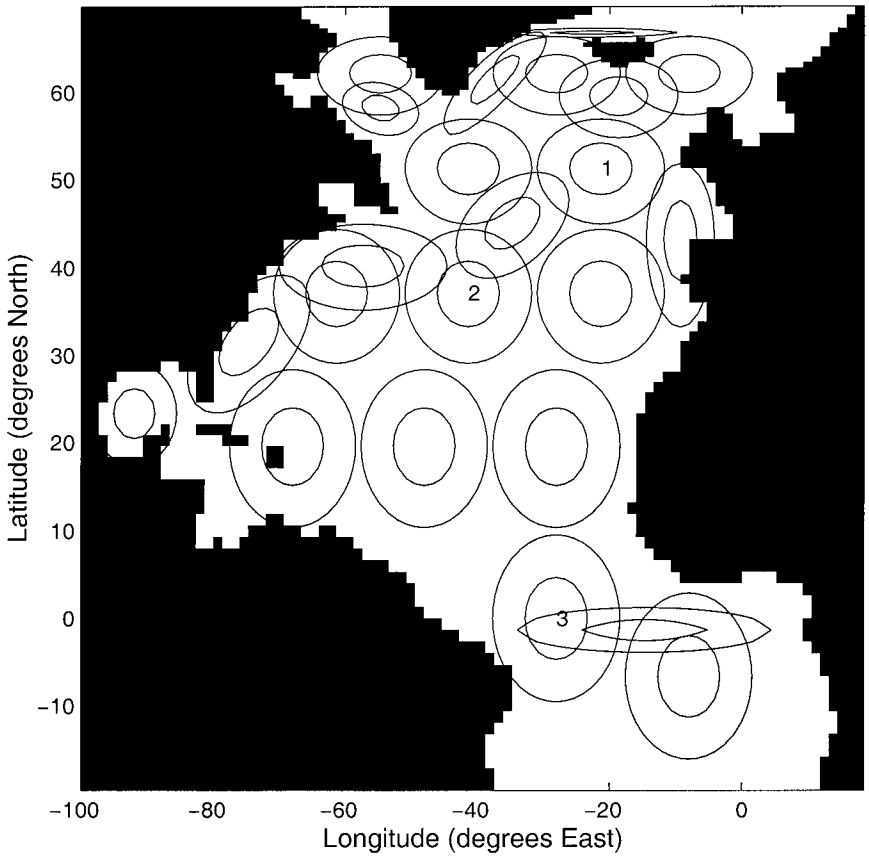

FIG. 6. Smeared impulse sources used to calculate the Green's function for the tracer equation in the GCM. The amplitudes of the individual Gaussian functions are contoured (with the inner and outer concentric ellipses having relative amplitudes of 0.8 and 0.4 units, respectively, compared to the center of each ellipse; amplitudes prior to normalization). Three positions, representative of regions and used in Fig. 8, are marked 1: North Eastern Atlantic, 2: Sargasso Sea, and 3: Tropics.

prior flux estimates are determined by partitioning the fields of spatial flux components into proportions associated with each Green's function component, accounting for the overlap in the impulse source functions. For inverse calculations using observations from a given simulation, the prior estimates used are those estimated from that simulation. For the inverse calculations using the real observations, the average of the prior estimates from the piston velocity parameterizations is used.

2) SURFACE CFC FLUX ERROR

If the flux equation (13) captures the complex turbulent processes through which tracer penetrates the ocean, then an estimate of the flux error can be obtained from the errors in the equation parameters. The solubilities and atmospheric tracer concentrations of the tracer species used are relatively well known (Warner and Weiss 1985; Walker et al. 2000; see also Meredith et al. 1996); in contrast, the piston velocity k has a large uncertainty. Asher and Wanninkhof (1998a) discuss this error stating that neither of the two parameterizations used here may be universally applicable due to the presence of naturally occurring surfactants. In particular, the relationship between k and the Schmidt number may vary with surface ocean conditions (e.g., calm or rough seas), causing errors of around 30% in the piston velocity for CFC-12 (this error is sensitive to the Schmidt number of the reference gas used for normalization). Another consideration is the poorly known effect of bubbles in air–sea tracer exchange for a gas near-equilibrium saturation. Using the data of Watson et al. (1991), Asher and Wanninkhof (1998b) found that including the effect of bubble gas transfer increased the piston velocities for helium by 20% (for a 10-m wind speed of 17 m s^{-1}). These results imply that there are significant errors (of at least 30%) associated with both piston velocity parameterizations considered here.

Correlations between different terms in (13) may act to reduce the overall error in the flux. The model CFC flux is a function of mixed layer CFC saturations and hence is controlled by the ability of the model to represent convective and ventilation processes. Where the flux of CFCs into the ocean is a relatively fast process

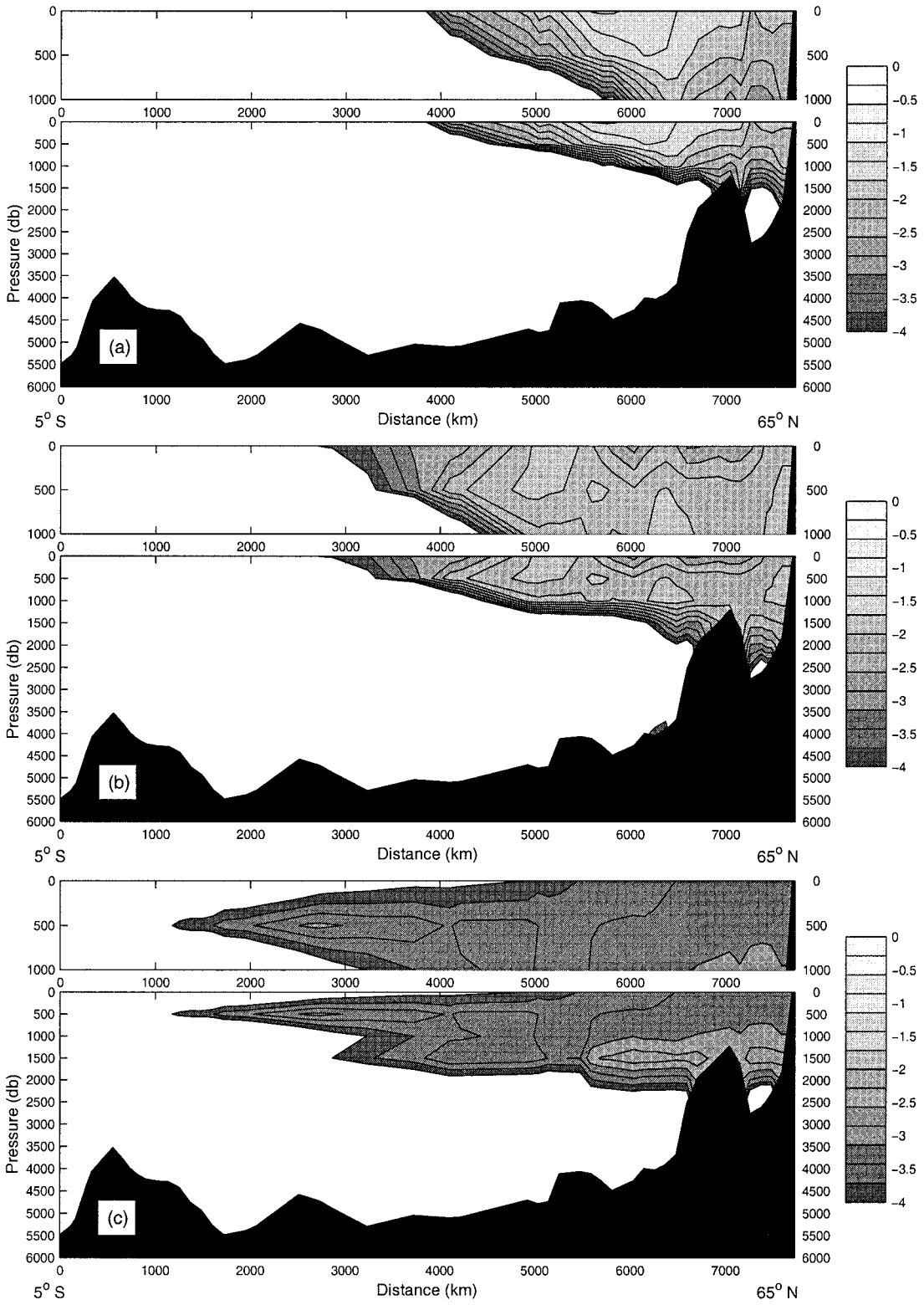

FIG. 7. Evolution of Green's function component ($\log_{10}$ units) with northeastern Atlantic source (see Fig. 6) along section shown in Fig. 1 where (a), (b), and (c) are after 1, 5, and 30 yr, respectively.

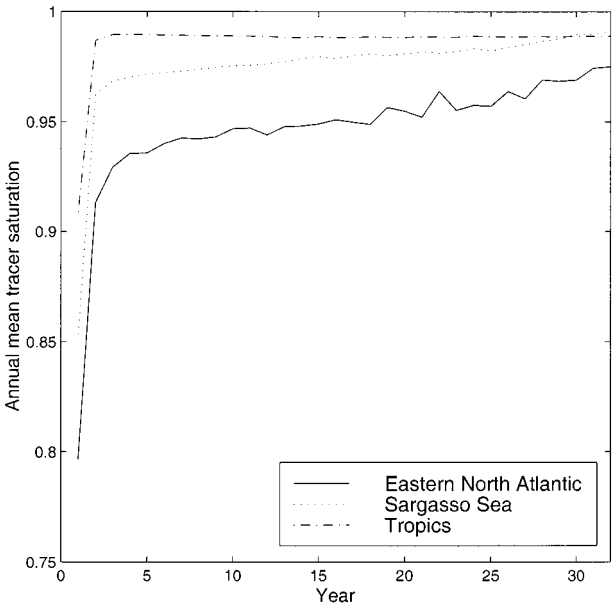

FIG. 8. Annual mean mixed layer CFC-11 saturation as a function of time at the three positions marked in Fig. 6 [from simulation with Wanninkhof (1992) piston velocity parameterization]. Year zero corresponds to 1962.

compared to the subduction of tracer into the ocean interior, then errors in the tracer saturation in the model mixed layer may, to some extent, compensate errors in the piston velocity, reducing the errors in the net simulated flux. For example, if near-equilibrium conditions are associated with high piston velocities, then this would act to oppose the tendency for high fluxes that would otherwise be associated with high piston velocities. However, this compensatory relationship is likely to break down in regions of deep convection. The combined effect on the surface flux error is difficult to estimate. On balance, we consider that a fractional flux uncertainty of 20%–50% is reasonable for our simulated CFC fluxes and derived prior flux estimates. A diagonal weight matrix, $\mathbf{P}_b$, is used for most of the inverse experiments. A nondiagonal form of $\mathbf{P}_b$, in which the fluxes of CFC-11 and CFC-12 are assumed to be correlated with a nominal correlation coefficient of 0.8, is also considered.

3) DATA ERROR

Two error sources in the tracer observations are considered: first, an instrumental error (typically 1%; Bullister and Weiss 1988) and, second, a sampling error representing the mesoscale variability in CFC fields, which cannot be captured by a coarse-resolution GCM (Haine and Gray 2000). Although this sampling error arises from the inability of the model to resolve mesoscale features, it can be treated as a data error. This error in the unresolved fields is then distinct from the error in the resolved circulation that we wish to determine.

The data error is defined as a fractional uncertainty with an absolute lower limit. Since oceanic CFC concentrations vary over several orders of magnitude, defining the data error in terms of a uniform fractional uncertainty places stronger fitting constraints on the weaker concentrations and, in the absence of a minimum data error, biases the fit towards these values. The fractional uncertainty used is based on work by Haine and Gray (2000), who suggest that the standard deviation in CFC concentrations on isopycnals due to sampling error may reach 50% in regions of strong eddy activity, dominating the smaller instrumental error. The data binning procedure smoothes the data somewhat and consequently the actual sampling error will be reduced in some grid boxes, although few grid boxes have more than ten measurements. Diagonal and nondiagonal forms of $\mathbf{P}_d$ are considered [the latter based on the analysis of the spatial correlations in ocean tracer fields by Haine and Gray (2000)]. Although these uncertainties are reasonable initial choices, more work is required to improve estimates of the variance of ocean tracer fields and to better exploit the information contained over the full range of measurable CFC concentrations.

d. Estimate of the method error

The method error is estimated by performing the inverse calculation using the synthetic CFC-11 and CFC-12 observations, section 3d(2). The eight inverse calculations performed (using both synthetic and real observations) are described in Table 3. Experiment S1 is the control inverse calculation using the synthetic data. Three experiments (S2–S4) were performed to determine the sensitivity of the inverse to the type of simulated data, specifically to the piston velocity parameterization used in the tracer simulation, and to whether the inverse calculation was performed separately for CFC-11 and CFC-12, or for both species together. The sensitivity of the inverse calculation to the number of components of the Green's function is investigated in experiment S5. The remaining inverse calculations (S6–S8) are designed to determine the minimum data and flux errors for which the null hypothesis $\mathcal{H}_0$ is satisfied.

The results of experiments S1–S8 are given in Tables 4 and 5. For each experiment, the weights are listed in the form of standard deviations for the data (including minimum values) and surface flux. For inversions that use both CFC-11 and CFC-12 measurements, two minimum data errors are given. These values are large enough that the inverse calculation is not strongly sensitive to them and are around 3% of the maximum data values for each species. The results of the inverse calculation are given in the form of values for the prior and posterior cost function and the goodness of fit, Q, (Table 4). Fractional residuals (mean and standard deviation) for the data and tracer flux (see section 3b) are

TABLE 3. Description of the inverse calculations: Expts S1–S8 use simulated data, and experiments R1–R8 use real data.

Expt	Description
S1	Control, simulated data: Wanninkhof (1992) parameterization for piston velocity, both tracer species [Data error is 20%, flux error is 20%, min. data error is 0.25 pmol kg^{-1} (CFC-11), 0.1 pmol kg^{-1} (CFC-12)]
S2	Liss and Merlivat (1986) parameterization for piston velocity, both tracer species
S3	Wanninkhof (1992) parameterization for piston velocity, CFC-11 only
S4	Wanninkhof (1992) parameterization for piston velocity, CFC-12 only
S5	Using first 13 Green's function components only [evenly distributed across the domain, equally sized and circular in gridpoint space (see Fig. 6)]
S6	Minimum data error reduced to 0.13 pmol kg^{-1} (CFC-11), 0.05 pmol kg^{-1} (CFC-12)
S7	Flux error decreased to 10%
S8	Data error decreased to 10%
R1	Control real data: Wanninkhof (1992) parameterization for piston velocity, both tracer species [Data error is 50%, flux error 20%, min. data error is 0.25 pmol kg^{-1} (CFC-11), 0.1 pmol kg^{-1} (CFC-12)]
R2	Using data from model layers 1-13 only (i.e., $\sigma_0 < 27.82$ kg m^{-3})
R3	Data error increased to 60%
R4	Flux error doubled to 40%
R5	Using off-diagonal elements in data weight matrix [see section 6c(3)]
R6	Using off-diagonal elements in flux weight matrix (correlation coefficient of 0.8 assumed between CFC-11 and -12 fluxes) [see section 6c(2)]
R7	Using off-diagonal elements in data and flux weight matrices (weight matrices as in R5 and R6, respectively)
R8	As R1 but solving for partial CFC concentrations and using appropriately increased minimum data errors (see section 6e)

given in Table 5. To be able to neglect the method error, the null hypothesis must be satisfied (Q large, randomly distributed residuals) for data and surface flux errors that are the same size or smaller than those estimated in the previous subsections [6c(3) and 6c(2)].

As expected, the quantitative results of the inverse calculation are insensitive to the piston velocity parameterization used to generate the simulated data (cf. experiments S1 and S2). The results of the inversion performed using the two simulated tracer species together (expt S1) agree with the results of performing the calculations individually (expts S3 and S4). The inverse calculation is fairly insensitive to the number of components of the Green's function used provided they provide adequate coverage of the domain. In experiment S5 only the first 13 components were used to determine the prior estimates of the fluxes and in the inverse calculation; these gave complete coverage with equally sized circular (in gridpoint space) impulse sources. This increased both the prior and posterior cost functions when compared with experiment S1 but still resulted in a good fit between the model and data. In contrast, reducing the number of components of the Green's function used to ten (such that they no longer provided complete coverage of the domain) markedly decreased the goodness of the fit between model and data and hence increased the method error (not shown). In this case the data error had to be increased to 100% to compensate, which implies that the method error was too large to be neglected.

The results of the remaining inverse calculations (S6–S8) show that a high probability of satisfying $\mathcal{H}_0$ exists ($Q \sim 1$ and relatively randomly distributed residuals, small bias, and standard deviation around unity) for pre-

TABLE 4. Results of the inverse calculation with the synthetic data (experiments S1–S8). Columns list prescribed fractional uncertainty in the data and flux (minimum data error in pmol kg^{-1}), the prior, $\mathcal{J}_{\text{prior}}$, and posterior cost function (decomposed into the data, $\mathcal{J}_d$, and flux, $\mathcal{J}_b$, costs), and the goodness of fit, Q ($\mathcal{J}$ and Q defined in section 3b; $Q = 1$ implies a good fit, whereas $Q = 0$ implies a bad fit). For details of the experiments see Table 3.

	Std dev						
Expt	Data	Min data[a]	Flux	$\mathcal{J}_{\text{prior}}$	$\mathcal{J}_d$[b]	$\mathcal{J}_b$[c]	Q
S1	20%	0.25, 0.1	20%	1.27×10^4	7.82×10^3	3.73×10^2	1
S2	20%	0.25, 0.1	20%	1.15×10^4	7.35×10^3	3.21×10^2	1
S3	20%	0.25	20%	6.79×10^3	3.83×10^3	2.08×10^2	1
S4	20%	0.1	20%	6.89×10^3	4.01×10^3	2.10×10^2	1
S5	20%	0.25, 0.1	20%	1.69×10^4	8.66×10^3	2.41×10^2	1
S6	20%	0.13, 0.05	20%	1.49×10^4	9.58×10^3	4.44×10^2	0.9
S7	20%	0.25, 0.1	10%	1.21×10^4	8.25×10^3	4.08×10^2	1
S8	10%	0.25, 0.1	20%	2.23×10^4	1.08×10^4	7.54×10^2	0

[a] Where two values, CFC-11 and CFC-12, otherwise appropriate to experiment (see Table 3).
[b] $\mathcal{J}_d[\hat{\mathbf{b}}] = (\mathbf{d} - \mathbf{G}_d\hat{\mathbf{b}})\mathbf{P}_d(\mathbf{d} - \mathbf{G}_d\hat{\mathbf{b}})$.
[c] $\mathcal{J}_b[\hat{\mathbf{b}}] = (\hat{\mathbf{b}} - \mathbf{b}_1)^T\mathbf{P}_b(\hat{\mathbf{b}} - \mathbf{b}_1)$.

TABLE 5. Results of the inverse calculation with the synthetic data (expts S1–S8). Columns list the mean and standard deviation of the fractional data and flux residuals (dimensionless, defined in section 3b). Negative residuals indicate that the observations exceed the posterior model prediction. For details of the experiments see Table 3.

	Residual	
Expt	Data	Flux
S1	−0.19 ± 0.85	−0.09 ± 2.88
S2	−0.17 ± 0.83	−0.10 ± 2.67
S3	−0.18 ± 0.84	−0.04 ± 3.07
S4	−0.19 ± 0.87	−0.01 ± 3.09
S5	−0.20 ± 0.90	−0.23 ± 3.10
S6	−0.22 ± 0.94	−0.08 ± 3.14
S7	−0.19 ± 0.88	−0.60 ± 2.95
S8	−0.17 ± 1.01	0.26 ± 4.09

TABLE 7. Results of the inverse calculation with the real data (expts R1–R8). Columns list the mean and standard deviation of the fractional data and flux residuals (dimensionless, defined in section 3b). Negative residuals indicate that the observations exceed the posterior model prediction. For details of the experiments see Table 3.

	Residual	
Expt	Data	Flux
R1	−0.62 ± 0.83	−0.07 ± 1.36
R2	−0.45 ± 0.77	−0.09 ± 1.29
R3	−0.54 ± 0.71	0.04 ± 1.09
R4	−0.62 ± 0.83	0.13 ± 1.56
R5	−0.62 ± 0.84	0.26 ± 2.43
R6	−0.62 ± 0.83	0.12 ± 1.92
R7	−0.61 ± 0.84	0.39 ± 3.12
R8	−0.62 ± 0.84	0.06 ± 1.30

scribed fractional data errors and flux errors of greater than ~20% (for minimum data errors of 0.25 and 0.1 pmol kg^{-1} for CFC-11 and -12, respectively). These data and flux errors are comparable to the real uncertainties, and the method error can thus be neglected when performing the inverse calculation with the real observations.

e. Testing the null hypothesis

The consistency of the model with the estimated surface CFC fluxes and CFC-11 and -12 observations can now be determined. The eight inverse calculations performed are labeled R1–R8 (Table 3). The control experiment R1 uses the best-guess weights and prior surface flux [estimated in sections 6c(2) and 6c(3)]. In the other experiments the effects of varying the weights, restricting the observations to those within the upper 13 of the 20 model layers, using nondiagonal data and flux errors, and solving the inverse calculation using the CFC partial pressure rather than the concentration are examined.

The results (Tables 6 and 7) show that the model is generally inconsistent with the observations and prior flux estimates because it fails the χ^2 test. An acceptable χ^2 can be achieved by relatively minor changes to the inversion parameters, however. For example, with a data error of 50% [the estimated uncertainty due to unresolved variability (Haine and Gray 2000)] there is inconsistency (expt R1). Restricting the observations to those just in the upper 13 model layers (i.e., $\sigma_0 < 27.82$ kg m^{-3}; shallower than about 2000 m) has a positive impact, yielding reduced prior and posterior cost functions, however. This now suggests a reasonable fit, although the bias in the data residuals is still relatively high (expt R2, see section 6f). The density range of these model layers includes the densities of all of the mode waters formed in the North Atlantic up to the density of the Labrador Sea water but excludes the densities of the North Atlantic Deep Water and Antarctic Bottom Water. Restricting the inverse calculation to those layers directly ventilated south of the Greenland–Scotland ridge in this way reduces the impact of the poor model representation of overflows (section 6a). Increasing the data error to 60% implies consistency (expt R3, $Q = 1$ and slightly reduced bias in the data residuals relative to expt R1). The inverse calculation is relatively insensitive to the error assumed for the

TABLE 6. Results of the inverse calculation with the real data using both tracer species (expts R1–R8). Columns list prescribed fractional uncertainty in the data and flux (minimum data error in pmol kg^{-1}, except for R8 where in pptv), the prior, $\mathcal{J}_{\text{prior}}$, and posterior cost function (decomposed into data, $\mathcal{J}_d$, and flux, $\mathcal{J}_b$, costs), and the goodness of fit, Q ($\mathcal{J}$ and Q defined in section 3b; $Q = 1$ implies a good fit, whereas $Q = 0$ implies a bad fit). For details of the experiments see Table 3.

	Std dev						
Expt	Data	Min data[a]	Flux	$\mathcal{J}_{\text{prior}}$	$\mathcal{J}_d$[b]	$\mathcal{J}_b$[c]	Q
R1	50%	0.25, 0.1	20%	1.14×10^4	1.11×10^4	8.35×10^1	0
R2	50%	0.25, 0.1	20%	8.35×10^3	8.09×10^3	7.51×10^1	1
R3	60%	0.25, 0.1	20%	8.36×10^3	8.19×10^3	5.40×10^1	1
R4	50%	0.25, 0.1	40%	1.14×10^4	1.10×10^4	1.10×10^2	0
R5	50%	0.25, 0.1	20%	1.75×10^4	1.66×10^4	2.68×10^2	0
R6	50%	0.25, 0.1	20%	1.14×10^4	1.11×10^4	9.38×10^1	0
R7	50%	0.25, 0.1	20%	1.75×10^4	1.66×10^4	2.74×10^2	0
R8	50%	12, 25	20%	1.15×10^4	1.13×10^4	7.64×10^1	0

[a] Two values, CFC-11 and CFC-12.
[b] $\mathcal{J}_d[\acute{\mathbf{b}}] = (\mathbf{d} - \mathrm{G}_d\acute{\mathbf{b}})^T\mathrm{P}_d(\mathbf{d} - \mathrm{G}_d\acute{\mathbf{b}})$.
[c] $\mathcal{J}_b[\acute{\mathbf{b}}] = (\acute{\mathbf{b}} - \mathbf{b}_1)^T\mathrm{P}_b(\acute{\mathbf{b}} - \mathrm{b}_1)$.

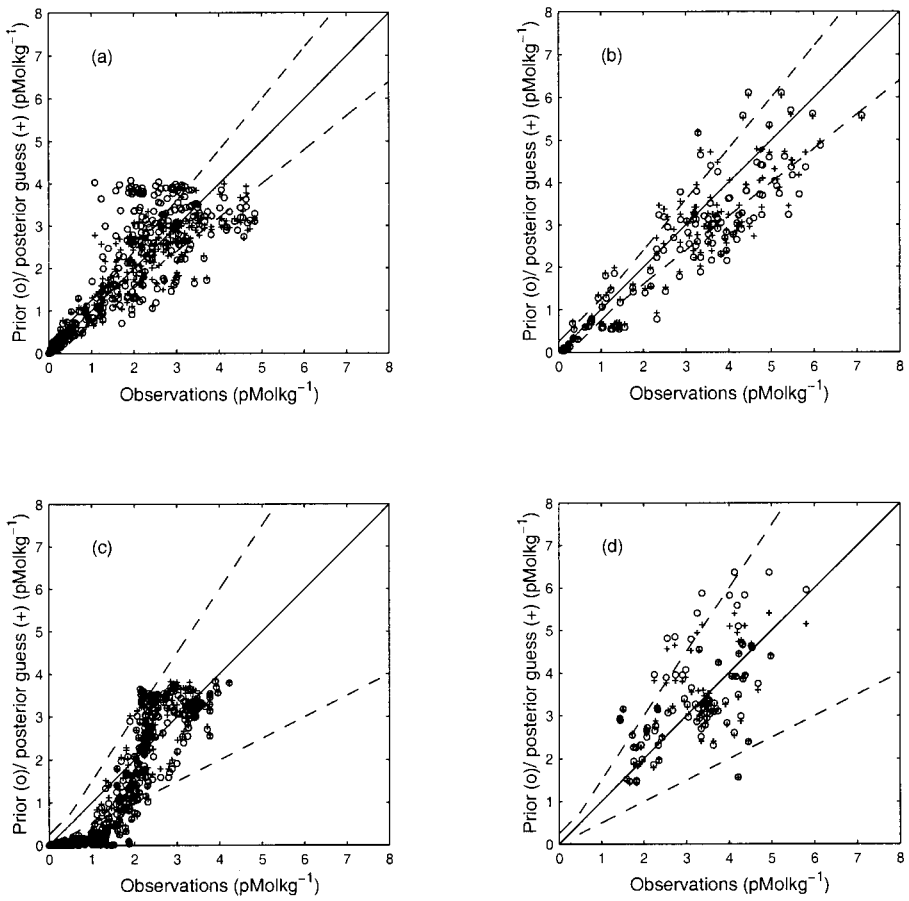

FIG. 9. Model CFC-11 concentration results, before and after inversion, compared to observations. (a) and (b) are for expt S1 (see Table 3) using synthetic data. In this case the only error arises from the Green's function method itself. (c) and (d) are for expt R2 (see Table 3) using real data and considering model layers 1–13 only ($\sigma_0 < 27.82$ kg m^{-3}). Results along the 20°W section (Fig. 1) are compared in (a) and (c), and results along the subpolar gyre section (Fig. 5) are compared in (b) and (d). In each case the circles and plus signs mark the prior and posterior results, respectively, the dashed lines show the expected range of error, and the full lines show perfect fits.

fluxes, since doubling them has little effect (expt R4). Similarly, the inclusion of nondiagonal data and flux covariances has little impact on the results (expts R5–R7). The prior and posterior cost functions increase, as do the bias and standard deviation in the flux residuals. However, the residuals show a smoother, more Gaussian, distribution (not shown). Finally, the inverse calculation was performed using CFC partial pressures, defined as CFC concentrations divided by solubility (Doney and Bullister 1992). If the fit to the partial pressure is significantly better than to the concentration, then the GCM ventilation rates may be correct but onto isopycnals with incorrect *T/S* properties. However, the relative improvement is slight, as the results (expt R8, minimum data error modified appropriately) are not significantly different to those of the comparable (same data and flux errors assumed) experiment, R1.

It is interesting that the inversions using real data (Table 6) show that allowing error in the air–sea CFC fluxes causes only a modest improvement in the cost function. This implies that the oceanic uptake of CFCs is more strongly controlled by the interior circulation than by the air–sea gas exchange. That is, the rate-limiting step in sequestration of CFCs is not surface transfer but interior redistribution. This suggests that, although they are uncertain, the current gas-transfer laws are adequate for estimating fluxes of rapidly transferred species such as CFCs.

f. The constrained fields

Figure 9 shows a selected comparison of CFC-11 model results with observations. For experiments S1 and R2 (Table 3) the model concentration, before and after inversion, is plotted against the observed measurement. Figures 9a and 9c are for the data along 20°W (Fig. 1), and Figs. 9b and 9d are for the data along the subpolar gyre section (Fig. 5). Overall, the posterior model results

show improved agreement with the data compared to the prior results, as they must to reduce the objective functional J. The posterior model results also satisfy the requirement that, on average, they do not differ from the observations more than the expected uncertainty (shown by the dashed lines). Notice also that the posterior results with the synthetic data (expt S1; Figs. 9a,b) are significantly better than those with real observations (expt R2; Figs. 9c,d). This means that the errors caused by an approximate inversion are less than those caused by data errors and/or deficiencies in the model transport, as discussed in section 6d. In this sense, our Green's function method is adequate for the present purposes.

The posterior model concentrations clearly show nonrandom structure on the 20°W section, however. We should therefore reject the null hypothesis for experiment R2, although the objective functional is acceptable in this case. The errors causing this structure are partly due to understandable deficiencies in the GCM. Some of the significant negative bias at low concentrations occurs in the Tropics and subtropics as a result of the southern model sponge layer. In other words, the model is not capturing the southern tracer sources that exist in reality [South Atlantic surface, Antarctic Intermediate and Antarctic Bottom Waters (Boebel et al. 1999; Schmitz 1995)]. The positive bias at high concentrations is partly a result of inadequate coverage of our discretized Green's function sources (Fig. 6). The same tendency can be seen in the S1 prior results (Fig. 9a). This stems from the fact that the 20°W section passes through the center of our Green's function sources in the extratropics. This causes a slight positive bias in the results on this section (if the section had passed between the Green's function sources we would expect a corresponding negative bias).

Although some of the residual structure in Fig. 9c arises from understandable GCM defects, systematic model–data differences are still apparent. These errors are also seen in Figs. 1a and 1b (the inversion improves these somewhat, as Fig. 9c shows). For example, the model excessively ventilates the water column to 1500 m over the Rockall plateau (near 7000 km on Fig. 1), causing the positive bias at high concentrations in Fig. 9c. It is also unable to adequately ventilate the subtropical Atlantic between 1500 and 2500 m (4000–6500 km on Fig. 1), causing the negative bias at low concentrations. These regional errors are important and are the topic of further study. At this stage we take the view that, although experiment R2 shows some residual structure after inversion, this does not appear to arise from major defects in the basin-scale model circulation. We therefore consider experiment R2 as a marginally inconsistent fit between the model and CFC data. That is, we do not find that the measurements fundamentally contradict the model solution; or, in other words, we believe only relatively minor changes are required to obtain a completely consistent fit.

The prior and constrained annual mean CFC-11 fluxes for 1982 are shown in Fig. 10. The fluxes that occurred in the forward simulations are shown in Fig. 10a (average of the two piston velocity parameterizations). Figure 10b shows the fluxes as reconstructed from the Green's function components using the prior estimates of the fluxes (for each Green's function component) determined from the forward simulations. The fluxes from the forward integration cannot be reconstructed precisely due to the limited number of Green's function components [part of the method error discussed in section 3d(2)]. Figure 10c shows the posterior fluxes as reconstructed from the Green's function components using the fluxes constrained by the observations (experiment R2). The most striking feature is a shift in the regions of strong fluxes with the fluxes into the Labrador Sea region decreased and those into the Denmark Strait region increased. The locally high fluxes in the Tropics (most in Fig. 10a) are evidence of another error in the Green's function method. They arise from the source of CFC-free waters at the southern boundary. Nevertheless, the impact on ventilation in the rest of the model domain is very weak.

7. Discussion: Limitations of results

There are several sources of error in our analysis in addition to the errors in the data, boundary flux, and Green's function method that have already been considered. In particular, the value of the results from the inverse calculations rests on the validity of the simplifying assumptions (section 3c). Here we review these sources of error and discuss the implications for our results. The interpretation of these results in terms of global-derived inventory and formation diagnostics is discussed in the next section.

Our assumption that the ocean is in a steady state is reasonable for aspects of ocean dynamics that vary on the much longer climatic timescales. However, the convective activity in the Sargasso, Labrador, and Greenland Seas are observed to have a strong decadal variability, which has been linked to the North Atlantic Oscillation (NAO: Dickson et al. 1996). In the 1960s, during a NAO minimum, ventilation in the Sargasso and Greenland Seas reached a maximum in contrast to the minimum in the Labrador Sea. More recently, the convective activity at these sites has reversed with maximum ventilation in the Labrador Sea contrasting with minimum ventilation in the Sargasso and Greenland Seas. The subduction of tracer into the main thermocline is probably associated with the strength of convection in the ventilation regions, so neglecting this time dependence is potentially important [as Doney et al. (1998) suggest] and will be a subject of further study. The El Nino–Southern Oscillation (ENSO) is observed to be associated with changes in sea surface temperatures in the Atlantic as well as in the Pacific (Curtis and Hastenrath 1995). ENSO may thus also affect ocean flows

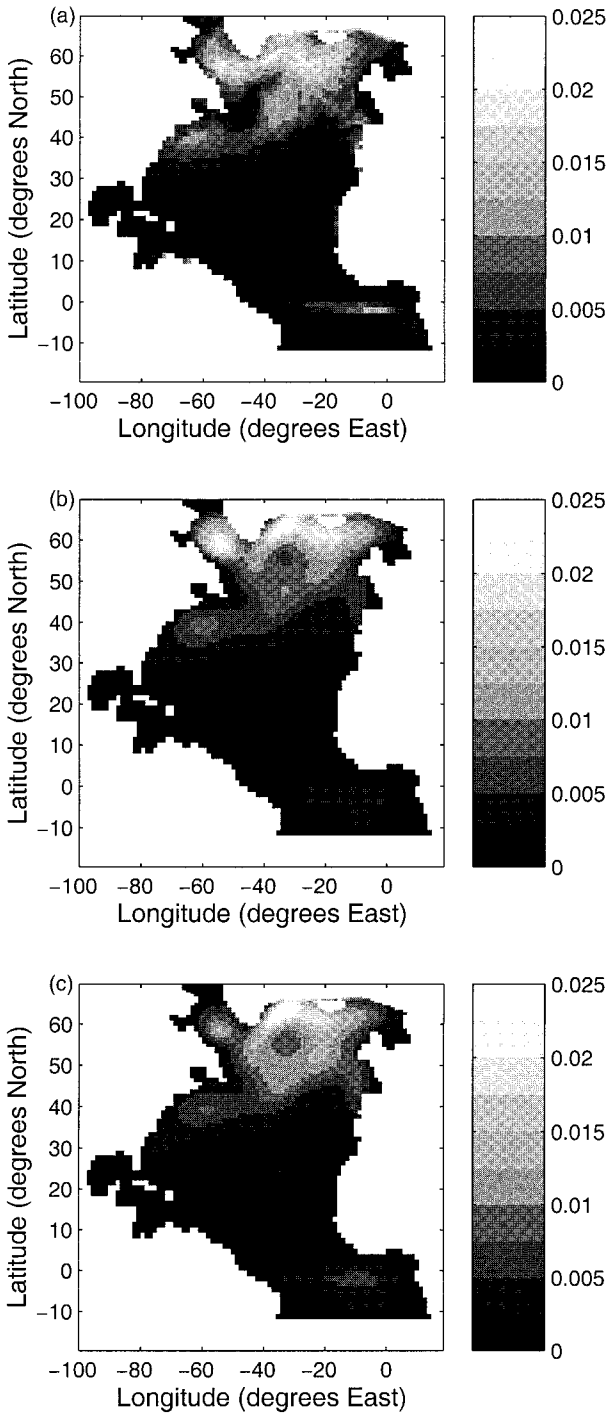

FIG. 10. Annual-mean CFC-11 fluxes for 1982 (grayscale units in pmol m^{-2} s^{-1}) (a) average of forward simulations with Wanninkhof (1992) and Liss and Merlivat (1986) piston velocity parameterizations, (b) reconstructed from Green's function components using priors (prior flux estimates used in the inverse calculations with the real observations), and (c) reconstructed from Green's function components using posteriors (constrained by inversion, expt R2 from Table 3). The estimated error in the prior flux estimates (for each Green's function component) is 20%. The error in the constrained fluxes (from experiment R2, for the Green's function components) is in the range 0.6%–18.3% (mean 7%). These fractional errors will be greater in the reconstructed fields [shown in (b) and (c)] at gridpoints where there is significant overlap of the Gaussian source functions. The prior and posterior CFC fluxes can be estimated for different years by multiplying the fields in (b) and (c) by the ratio of the tropospheric CFC mixing ratio in the desired year to the 1982 value (see Fig. 4).

and the uptake of atmospheric tracers, even in the Atlantic, with a shorter timescale of around 2–7 years.

The flux boundary condition was separated into independent spatial and temporal components and the mixed layer saturation was also assumed to be constant on interannual timescales. Even for a steady-state ocean these assumptions are only valid for certain tropospheric source functions, and this assumption is an approximation for the CFCs considered (Fig. 8). An obvious example of a tracer for which this assumption would have no validity is anthropogenic tritium. This species entered the atmosphere during the bomb tests of the 1950s and 1960s and since then its atmospheric concentration has slowly decayed (Doney and Jenkins 1988). Hence, while initially the net tritium flux was into the ocean (saturations less than unity), the net flux is now reversed (saturations greater than unity). An alternative approach, in which a separable flux is still assumed, is to calculate the time dependence of the tracer flux from the model simulation (which would be slightly different from the atmospheric tracer history). This was rejected here because this tracer flux is model dependent and an unreliable indicator of the true time dependences of observed fluxes.

Constraining a GCM using prior surface fluxes estimated from the same GCM may appear ill advised. Nevertheless, direct measurement of tracer fluxes is extremely difficult. An alternative approach is to estimate them indirectly using the flux equation and field observations. A particular disadvantage to this approach is that surface saturations are strong functions of position and season. The seasonality can be clearly seen in results from a one-dimensional slab mixed layer model (Haine and Richards 1995) and in a global GCM (Craig et al. 1998). Observations are biased towards high saturations since the lowest saturations generally occur at high latitudes during deep winter convection when measurements are rarely made. It is thus difficult to obtain reasonable estimates of annual-mean tracer fluxes from observations.

The neglect of tracer transport across the northern and southern boundaries also deserves further discussion. Additional Green's function components can be calculated to represent these transports, but reasonable prior estimates of the transports are required to use them in the inverse calculation. Test calculations have shown that Green's function components representing tracer advection across the northern boundary do not penetrate far into the interior during the 32-yr period (not shown). However, there is some transport across Denmark Strait

into the Labrador Sea (in all density layers). There is little transport into the domain across the Iceland–Scotland Ridge. A Green's function component representing tracer advection across the southern boundary shows that water masses crossing this boundary spread over the entire domain within 15–20 years via a route up the western boundary. However, the main interior water masses (Antarctic Intermediate and Bottom Waters) are old by the time they cross this boundary and contain small concentrations of CFCs (Fig. 1a). This model error can be treated as a data error by increasing the data error on the observations in the vicinity of the northern and southern boundaries. Tests (not shown) found that this did not lead to a significant improvement in the fit obtained in the inverse calculation when compared with the effect of increasing the data error by the same amount on the same number of randomly selected observations. We therefore conclude that, while neglecting tracer transport across the northern and southern boundaries is not ideal (and biases the residuals, section 6f), it appears unlikely to have a strong impact on our conclusions. This neglect is preferable to attempting to estimate the prior estimates of these transports, which would be needed to represent them in the inverse calculation.

It is possible that we have incorrectly estimated the number of degrees of freedom because of correlations between observations or fluxes (section 3b). In fact, when we use our recent estimate for the nondiagonal data covariances (Haine and Gray 2000), the results only change slightly (expts R5 and R7, Table 6). The nondiagonal data covariance is full rank, so the data still contribute independently. Similarly, the nondiagonal flux covariances have a minor impact (expts R6 and R7). Nevertheless, the spatial correlation estimates of Haine and Gray (2000) are themselves uncertain. An alternative test is to repeat experiment R2 using a subset of widely spaced data locations. In this case, the relative fit is slightly improved, suggesting that the GCM captures the larger scales somewhat better than small scales. However, there is no indication that the number of degrees of freedom has been seriously misjudged. We emphasize that this method yields a single measure of the consistency of the model circulation with the observations and does not directly provide information on the cause of inconsistencies.

Finally, while processing the CFC data (section 4), we used density as the vertical coordinate, the natural choice for MICOM. Alternatively, pressure could be used, the natural choice for a z-coordinate model. Where the model density field is erroneous, extra uncertainty can be introduced this way. For example, Fig. 1 shows near-surface CFC-11 isopleths shoaling at the equator, whereas the model field does not. Some, but not all, of this discrepancy is compensated for in our isopycnal analysis because the model layers are also too flat (not shown). In other words, some of the posterior model/data misfit may be due to a good model CFC distribution in depth masked by a deficient model density field. Nevertheless, it is unlikely that this can explain the residual structure shown in Fig. 9c.

8. Discussion: Interpretation of results

This systematic attempt to combine observations with a model circulation has shown the model circulation to be marginally inconsistent with the CFC observations, prior flux estimates, and the estimated errors in these quantities when the effects of unresolved variability are considered; that is, the inverse almost satisfies the null hypothesis, $\mathcal{H}_0$. This can be compared with recent work by Heinze et al. (1998), who concluded that CFCs, anthropogenic tritium, and tritiugenic helium-3 are inconsistent with a 3.5°-resolution global GCM. Nevertheless, despite the limitations of this approach, outlined in section 7, the observations constrain the model to some extent. We consider the agreement obtained in the best-fit experiment (R2) to be sufficiently good that the constrained circulation is of interest and can provide useful information about the North Atlantic circulation. In particular, global diagnostics are likely to be least sensitive to the region-specific errors in the model circulation. Such diagnostics are required to provide a balanced discussion of our results and are relevant model quantities for future comparison.

We have examined the overall ventilation in the constrained circulation. The tracer inventory is an important average quantity in this regard, which may be easily diagnosed using the model Green's function. The inventory, I_V, is the total amount of tracer substance in a volume V:

$$I_V(t) = \int_V C(\mathbf{x}, t)\, dV. \tag{23}$$

This quantity may be calculated from the Green's function [see (11)],

$$I_V(t) = \int_V \int_0^t \int_{S_1} G(\mathbf{x}, t; \mathbf{x}_S, t_0) B_N(\mathbf{x}_S, t_0)\, dS\, dt_0\, dV, \tag{24}$$

for any given boundary flux B_N. These integrations are performed directly using the archived Green's function for the MICOM model for various isopycnal layers and times during the CFC transient. Figure 11a shows the total inventory of CFC-11 as a function of time. The total inventory in density classes directly ventilated in the North Atlantic south of the Greenland–Scotland ridge is shown in Fig. 11b. There is reasonable consistency with the calculations of Smethie and Fine (2001) and Rhein et al. (2000). Craig et al. (1998) estimate a global uptake of 2.7×10^8 mol of CFC-11 in 1990 based on a 1°-resolution GCM. Our results suggest that 22% of this enters the North Atlantic Ocean, twice the global average value. The tracer is being absorbed in the seasonally mixed surface layers and in the two prin-

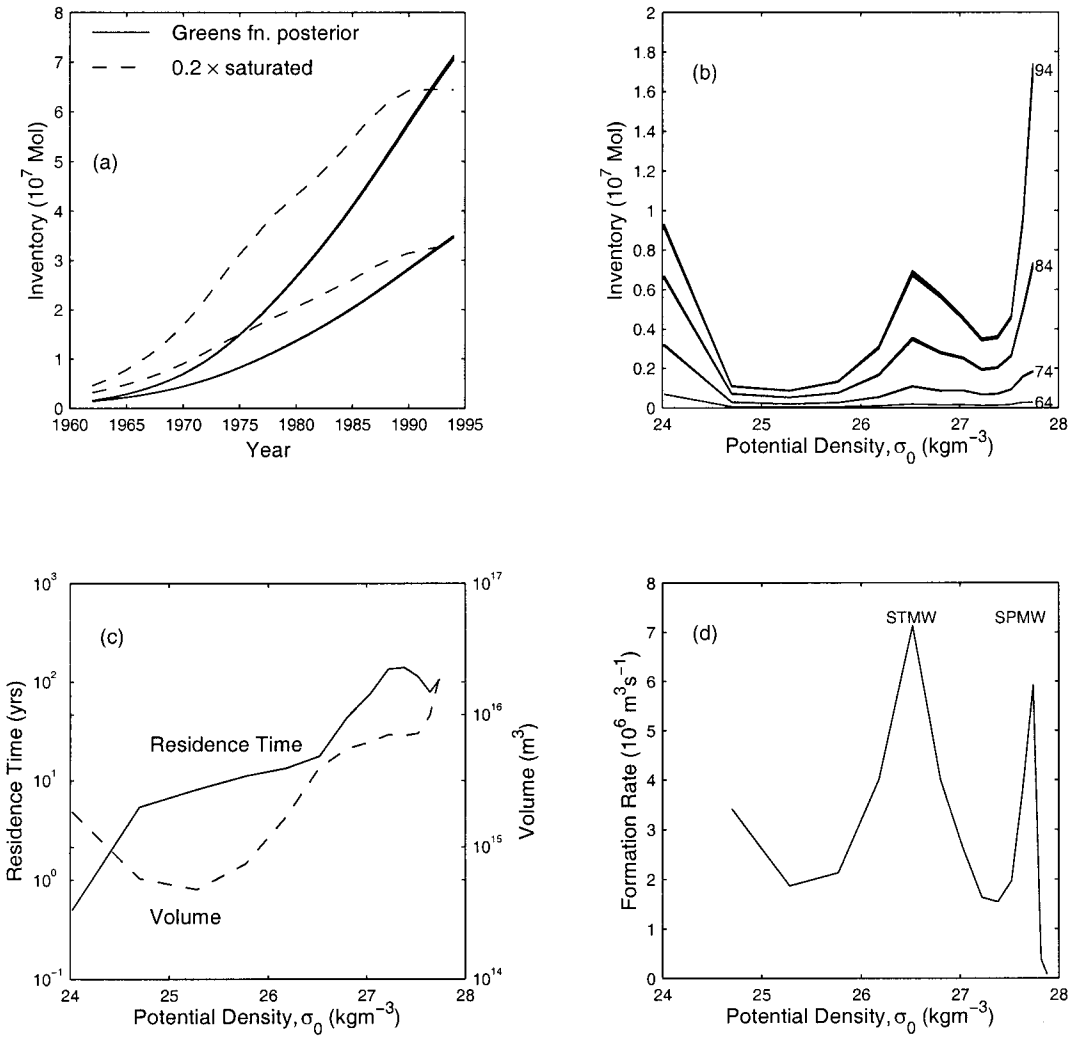

FIG. 11. (a) North Atlantic CFC-11 (upper) and CFC-12 (lower) inventory (10^7 mol) for densities less than $\sigma_0 = 27.82$ kg m^{-3} using the results of expt R2. The dashed line shows the inventory for this volume at 20% equilibrium saturation. (b) CFC-11 inventory for $\sigma_0 < 27.82$ kg m^{-3} as a function of density for years 1964, 1974, 1984, and 1994. (c) Residence time (yr) as a function of density based on a simple box mixing model and the CFC-11 results of expt R2. A saturation of 0.9 is assumed at the time of permanent subduction. The volume (m^3) of each density class is also shown. (d) Formation rate (10^6 m^3 s^{-1}) calculated from the CFC inventory. STMW is subtropical mode water and SPMW is subpolar mode water; see text for details. The thickness of the full lines indicates the posterior error from the inversion.

cipal mode waters formed in the North Atlantic: Subtropical Mode Water (STMW; $\sigma_0 \approx 26.5$ kg m^{-3}) and Subpolar Mode Water (SPMW; $\sigma_0 \approx 27.75$ kg m^{-3}) (Speer and Tziperman 1992). Taking all the waters lighter than $\sigma_0 = 27.82$ kg m^{-3} (pressures less than about 2000 db, layers 1 to 13) together, the North Atlantic Ocean was near 20% saturated with CFC in the mid-1990s.

The corresponding residence time is calculated using a simple box mixing model (Fig. 11c) and, hence, typical ventilation rates are estimated. We use a saturation at subduction of 0.9 as an average over the North Atlantic for this calculation [based on an average mixed layer depth of a few hundred meters and the results of Haine and Richards (1995)]. The subduction rates, averaged over the last 20–30 yr and based on our synthesis of CFC data and the MICOM circulation, are shown in Fig. 11d. The formation of STMW and SPMW with peak rates around 6–7 Sv (Sv $\equiv 10^6$ m^3 s^{-1}) is clear. Recent results by Rhein et al. (2000) show good agreement for the subpolar formation rates. It is also remarkably consistent with the estimates of Speer and Tziperman (1992) based on an independent surface buoyancy analysis. Interestingly, their analysis suggests no formation between the two mode waters. Our estimate is about 1.5 Sv at $\sigma_0 = 27.3$ kg m^{-3} and may be due to processes (such as interior diabatic mixing and lateral transfers in the mixed layer) that are very hard to estimate using other methods [see also Sarmiento (1983)].

9. Conclusions

We have developed and tested an inverse method for constraining ocean general circulation models using transient tracer observations. The method has been implemented in a North Atlantic configuration of the Miami Isopycnic Coordinate Ocean Model with $\frac{1}{3}^\circ$ resolution. A substantial quantity of North Atlantic CFC-11 and CFC-12 data has been collated for the period 1982–1994, and the fluxes of these tracers into the ocean and the errors in the fluxes and in the tracer data have also been estimated.

Systematic differences can be seen between the observed CFC concentrations and a prior prediction of these concentrations by the model. In particular, tracer plumes in overflows such as the Denmark Strait overflow are not well represented in the model. The inverse method determines the likelihood that these differences occurred by chance, given that the air–sea transfer of CFC is itself uncertain. Our method assumes that the model is perfect, and then the validity of this assumption is examined by determining the optimum air–sea CFC flux using the Green's function for the model passive tracer equation.

The principal sources of error in the analysis are the assumption of a steady ocean state and the neglect of tracer fluxes across open boundaries. Despite these uncertainties we find that the model tracer field is only marginally inconsistent with the CFC observations on surfaces less dense than $\sigma_0 = 27.82$ kg m^{-3} (those isopycnals directly ventilated in the open North Atlantic, shallower than about 2000 m). That is, we almost satisfy the null hypothesis that the model and observations are consistent when the effects of unresolved variability are taken into account. There are some systematic biases in the model − data differences that identify model shortcomings in the subpolar gyre. Consequently, the CFC observations constrain the model to some extent, but there do not appear to be any gross errors in the basin-scale model tracer field. Using the constrained CFC fields the net North Atlantic ventilation is estimated. There is good general agreement with independent prior results. The disparities are also interesting, as they might be caused by interior water mass formation mechanisms.

The next stage is to repeat the inverse calculation with a modified model circulation and extended dataset. This approach allows improvements in the circulation to be quantified as the fit with the observations varies. The simple interpretation of Green's functions in terms of the classical oceanographic concepts of water mass analysis and age (section 2) may guide beneficial changes to the model circulation.

Acknowledgments. We thank Chantal Andrié, John Bullister, Scott Doney, Rana Fine, Elisabet Fogelqvist, Monika Rhein, Bill Smethie, Denise Smythe-Wright, Rik Wanninkof, Mark Warner, and Ray Weiss who kindly provided their tracer measurements for this study. Yan Li Jia and Kelvin Richards helped us use the MICOM model. This work was supported by Grant GST/02/1685 of the U.K. Natural Environment Research Council.

APPENDIX A

Derivation of the Green's Function Solution to the Tracer Equation

The Green's function $G(\mathbf{x}, t; \mathbf{x}_0, t_0)$ is the solution to the inhomogeneous tracer equation (5) with homogeneous boundary conditions (6). It satisfies two important relationships, causality and reciprocity. Causality is expressed as

$$G(\mathbf{x}, t; \mathbf{x}_0, t_0) = 0 \quad \text{if } t < t_0. \tag{A1}$$

This physically *imposed* condition implies that the Green's function uniformly vanishes for all times prior to the impulsive delta function. Reciprocity is expressed as

$$G(\mathbf{x}, t; \mathbf{x}_0, t_0) = G^\dagger(\mathbf{x}_0, t_0; \mathbf{x}, t), \tag{A2}$$

where the adjoint Green's function, $G^\dagger$, satisfies the corresponding adjoint advection–diffusion equation,

$$-\frac{\partial G^\dagger}{\partial t} - \mathbf{u}\cdot\boldsymbol{\nabla}G^\dagger - \boldsymbol{\nabla}\cdot(\kappa\boldsymbol{\nabla}G^\dagger) = \delta(\mathbf{x} - \mathbf{x}_0, t - t_0). \tag{A3}$$

This time-reversed problem satisfies the same boundary conditions as G, while the initial conditions for $G^\dagger$ are given by an adjoint causality relation:

$$G^\dagger(\mathbf{x}_0, t_0; \mathbf{x}, t) = 0 \quad \text{if } t < t_0. \tag{A4}$$

The solution to the tracer equation is found by multiplying (A3) by C and subtracting this from (1) multiplied by $G^\dagger$ (forming Green's identity). Integrating over all space and time gives

$$\int_0^{t^+}\int_R G^\dagger\left[\frac{\partial C}{\partial t} + \mathbf{u}\cdot\boldsymbol{\nabla}C - \boldsymbol{\nabla}\cdot(\kappa\boldsymbol{\nabla}C)\right] + C\left[\frac{\partial G^\dagger}{\partial t} + \mathbf{u}\cdot\boldsymbol{\nabla}G^\dagger + \boldsymbol{\nabla}\cdot(\kappa\boldsymbol{\nabla}G^\dagger)\right] dt\, dV = \int_0^{t^+}\int_R G^\dagger q - C\delta(\mathbf{x} - \mathbf{x}_0, t - t_0)\, dt\, dV, \tag{A5}$$

where t^+ is marginally greater than t. The left-hand side of this expression can be written

$$\int_0^{t^+} \int_R \frac{\partial(G^\dagger C)}{\partial t} + \mathbf{u} \cdot \boldsymbol{\nabla}(G^\dagger C) + \boldsymbol{\nabla} \cdot [\kappa(C\boldsymbol{\nabla}G^\dagger - G^\dagger \boldsymbol{\nabla}C)]\, dt\, dV. \tag{A6}$$

The first term may be integrated once directly, while the divergence theorem applies to the second and third terms assuming nondivergent flow, which yields

$$\int_R [G^\dagger C]_0^{t^+}\, dV + \int_0^{t^+} \int_S [(G^\dagger C)\mathbf{u} + \kappa(C\boldsymbol{\nabla}G^\dagger - G^\dagger \boldsymbol{\nabla}C)] \cdot \mathbf{n}\, dS\, dt. \tag{A7}$$

The first integrand in the second expression clearly vanishes since there is no normal flow through S. Finally, the second term on the right-hand side of (A5) can be explicitly integrated to give $C(\mathbf{x}_0, t_0)$. An expression for $C(\mathbf{x}, t)$ is written by relabeling and use of the reciprocity theorem to replace $G^\dagger$ with G, yielding

$$C(\mathbf{x}, t) = \int_0^t \int_R G(\mathbf{x}, t; \mathbf{x}_0, t_0) q(\mathbf{x}_0, t_0)\, dt_0\, dV_0 + \int_R G(\mathbf{x}, t; \mathbf{x}_0, 0) I(\mathbf{x}_0)\, dV_0 + \int_0^t \int_S \{G(\mathbf{x}, t; \mathbf{x}_S, t_0) B_N(\mathbf{x}_S, t_0) - \kappa(\mathbf{x}_S, t_0)[\boldsymbol{\nabla}_0 G(\mathbf{x}, t; \mathbf{x}_S, t_0) \cdot \mathbf{n}] B_D(\mathbf{x}_S, t_0)\}\, dS_0\, dt_0. \tag{A8}$$

APPENDIX B

Derivation of the Optimal Boundary Condition

The expression for the objective functional (16) can be rewritten using (12) and (11) to yield

$$\mathcal{J}[b] = (\mathbf{d} - G_d \circ b)^{\mathrm{T}} \mathbf{P}_d (\mathbf{d} - G_d \circ b) + (b - b_1) \circ P_b \circ (b - b_1), \tag{B1}$$

where the $\circ$ operator is used as shorthand for integration over S and t. Here $G_d = G(\mathbf{x}_d, t_d; \mathbf{x}_0, t_0)$, the Green's function at the locations of the observations arranged in an $M \times 1$ column vector. The minimum of the objective functional $\mathcal{J}$ is given by the optimal choice of boundary condition, $\hat{b}$. It can be found by writing

$$\mathcal{J}[\hat{b} + \delta b] = \mathcal{J}[\hat{b}] + O(\delta b^2) \tag{B2}$$

for a small perturbation, δb. Thus,

$$\delta\mathcal{J} = \mathcal{J}[\hat{b} + \delta b] - \mathcal{J}[\hat{b}] = 2(G_d \circ \delta b)^{\mathrm{T}} \mathbf{P}_d (G_d \circ \hat{b} - \mathbf{d}) + 2\delta b \circ P_b \circ (\hat{b} - b_1) + O(\delta b^2). \tag{B3}$$

Now the assertion that $\delta\mathcal{J} = O(\delta b^2)$ so that the coefficients multiplying δb in (B3) must vanish uniformly requires that

$$G_d^{\mathrm{T}} \mathbf{P}_d (G_d \circ \hat{b} - \mathbf{d}) + (\hat{b} - b_1) \circ P_b = 0, \tag{B4}$$

and so

$$(G_d^{\mathrm{T}} \mathbf{P}_d G_d + P_b) \circ \hat{b} = G_d^{\mathrm{T}} \mathbf{P}_d \mathbf{d} + P_b \circ b_1. \tag{B5}$$

REFERENCES

Andrié, C., J. F. Ternon, M. J. Messias, L. Memery, and B. Bourlès, 1998: Chlorofluoromethane distributions in the deep equatorial Atlantic during January–March 1993. *Deep-Sea Res.* (Part I), **45,** 903–929.

Asher, W., and R. Wanninkhof, 1998a: Transient tracers and air–sea gas transfer. *J. Geophys. Res.*, **103,** 15 939–15 958.

——, and ——, 1998b: The effect of bubble-mediated gas transfer on purposeful dual-gaseous tracer experiments. *J. Geophys. Res.*, **103,** 10 555–10 560.

Bleck, R., and L. T. Smith, 1990: A wind-driven isopycnic coordinate model of the North and equatorial Atlantic Ocean. I. Model development and supporting experiments. *J. Geophys. Res.*, **95,** 3273–3285.

——, H. H. Hanson, D. Hu, and E. B. Kraus, 1989: Mixed layer–thermocline interaction in a 3D isopycnic coordinate model. *J. Phys. Oceanogr.*, **19,** 1417–1439.

——, C. Rooth, D. Hu, and L. T. Smith, 1992: Salinity-driven thermocline transients in a wind- and thermohaline-forced isopycnic coordinate model of the North Atlantic. *J. Phys. Oceanogr.*, **22,** 1486–1505.

Boebel, O., R. E. Davis, M. Ollitrault, R. G. Peterson, P. L. Richardson, C. Schmid, and W. Zenk, 1999: The intermediate depth circulation of the western South Atlantic. *Geophys. Res. Lett.*, **26,** 3329–3332.

Bullister, J. L., and R. F. Weiss, 1988: Determination of $CC_{13}F$ and $CC_{12}F_2$ in seawater and air. *Deep-Sea Res., Part A,* **35,** 839–853.

Castle R., and Coauthors, 1997: Chemical and hydrographic profiles and underway measurements from the eastern North Atlantic

during July and August of 1993. NOAA Data Rep. ERL AOML-32, 82 pp. [NTIS PB98-131865INZ.]

Craig, A. P., J. L. Bullister, D. E. Harrison, R. M. Chervin, and A. J. Semtner Jr., 1998: A comparison of temperature, salinity, and chlorofluorocarbon observations with results from a 1° resolution three-dimensional global ocean model. *J. Geophys. Res.*, **103,** 1099–1119.

Curtis, S., and S. Hastenrath, 1995: Forcing of anomalous sea surface temperature evolution in the tropical Atlantic during Pacific warm events. *J. Geophys. Res.*, **100,** 15 835–15 847.

da Silva, A., A. C. Young, and S. Levitus, 1994: *Atlas of Surface Marine Data 1994,* Vol. 1: *Algorithms and Procedures*, NOAA Atlas NESDIS 6.

Dickson, R., J. Lazier, J. Meincke, P. Rhines, and J. Swift, 1996: Long-term coordinated changes in the convective activity of the North Atlantic. *Progress in Oceanography,* Vol. 38, Pergamon, 241–295.

Dixon, K. W., J. L. Bullister, R. H. Gammon, and R. J. Stouffer, 1996: Examining a coupled climate model using CFC-11 as an ocean tracer. *Geophys. Res. Lett.*, **23,** 1957–1960.

Doney, S. C., and W. J. Jenkins, 1988: The effect of boundary conditions on tracer estimates of thermocline ventilation rates. *J. Mar. Res.*, **46,** 947–965.

——, and J. L. Bullister, 1992: A chlorofluorocarbon section in the eastern North Atlantic. *Deep-Sea Res.* (Part I), **39,** 1857–1883.

——, ——, and R. Wanninkof, 1998: Climatic variability in upper ocean ventilation rates diagnosed using chlorofluorocarbons. *Geophys. Res. Lett.*, **25,** 1399–1402.

DYNAMO Group, 1997: Final scientific report. Berichte aus dem Institut fur Meereskunde an der Universitat Kiel 294, 334 pp.

Elkins, J. K., T. M. Thompson, T. H. Swanson, J. H. Butler, B. D. Hall, S. O. Cummings, D. A. Fisher, and A. G. Raffo, 1993: Decrease in the growth-rates of atmospheric chlorofluorocarbon-11 and chlorofluorocarbon-12. *Nature,* **364,** 780–783.

Griffiths, G., and Coauthors 1992: CTD oxygen, tracer and nutrient data from RRS Charles Darwin cruises 58/59 in the NE Atlantic as part of Vivaldi '91. IOSDL Rep. 296, 48 pp. [Available from Library, SOC, Empress Dock, Southampton S014 3ZH, United Kingdom.]

Haine, T. W. N., and K. J. Richards, 1995: The influence of the seasonal mixed layer on oceanic uptake of CFCs. *J. Geophys. Res.*, **100,** 10 727–10 744.

——, and S. L. Gray, 2000: Quantifying mesoscale variability in transient tracer fields. *J. Geophys. Res.*, in press.

Hall, T. M., and R. A. Plumb, 1994: Age as a diagnostic of stratospheric transport. *J. Geophys. Res.*, **99,** 1059–1070.

Heinze, C., E. Maier-Reimer, and P. Schlosser, 1998: Transient tracers in a global OGCM: Source functions and simulated distributions. *J. Geophys. Res.*, **103,** 15 903–15 922.

Hogg, N. G., R. S. Pickart, R. M. Hendry, and W. M. Smethie Jr., 1986: The northern recirculation gyre of the Gulf Stream. *Deep-Sea Res.* (Part I), **33,** 1139–1165.

Holzer, M., and T. M. Hall, 2000: Transit-time and tracer-age distributions in geophysical flows. *J. Atmos. Sci.*, **57,** 3539–3558.

Jenkins, W. J., 1988: The use of anthropogenic tritium and He-3 to study sub-tropical gyre ventilation and circulation. *Phil. Trans. Roy. Soc. London,* **325A,** 43–61.

Jia, Y., 2000: Formation of an Azores current due to Mediterranean overflow in a modeling study of the North Atlantic. *J. Phys. Oceanogr.*, **30,** 2342–2358.

——, and K. J. Richards, 1996: Tritium distributions in an isopycnic model of the North Atlantic. *J. Geophys. Res.*, **101,** 11 883–11 901.

Kraus, E. B., and J. S. Turner, 1967: A one-dimensional model of the seasonal thermocline. Part II: The general theory and its consequences. *Tellus,* **19,** 98–105.

Levitus, S., 1982: *Climatological Atlas of the World Ocean.* NOAA Prof Paper No. 13, U.S. Govt. Printing Office, 173 pp and 17 microfiche.

Liss, P. S., and L. Merlivat, 1986: Air–sea gas exchange rates: Introduction and synthesis. *The Role of Air–Sea Exchange in Geochemical Cycling,* P. Buat-Menard, Ed., D. Reidel, 113–127.

McKee, T. K., R. S. Pickart, W. M. Smethie Jr., and W. J. Jenkins, 1995: Hydrographic data from ENDEAVOR 223: Formation and spreading of the shallow component of the North Atlantic deep western boundary current. WHOI Tech. Rep. WHOI-95-07, Woods Hole Oceanographic Institution, Woods Hole, MA, 119 pp.

Meméry, L., and C. Wunsch, 1990: Constraining the North Atlantic circulation with tritium data. *J. Geophys. Res.*, **95,** 5239–5256.

Meredith, M. P., K. A. VanScoy, A. J. Watson, and R. A. Locarnini, 1996: On the use of carbon tetrachloride as a transient tracer of Weddell Sea deep and bottom waters. *Geophys. Res. Lett.*, **23,** 2943–2946.

Morse, P. M., and H. Feshbach, 1953: *Methods of Theoretical Physics.* Part I. McGraw-Hill, 997 pp.

New, A. L., R. Bleck, Y. Jia, R. Marsh, M. Huddleston, and S. Barnard, 1995: An isopycnic model study of the North Atlantic. Part I: Model experiment. *J. Phys. Oceanogr.*, **25,** 2667–2699.

Oreskes, N., K. Shrader-Frechette, and K. Berlitz, 1994: Verification, validation, and confirmation of numerical-models in the Earth sciences. *Science*, **263,** 641–646.

Pickart, R. S., and W. M. Smethie Jr., 1993: How does the deep boundary current cross the Gulf Stream? *J. Phys. Oceanogr.*, **23,** 2602–2616.

——, N. G. Hogg, and W. M. Smethie Jr., 1989: Determining the strength of the Deep Western Boundary current using the chlorofluoromethane ratio. *J. Phys. Oceanogr.*, **19,** 940–951.

——, T. K. McKee, and W. M. Smethie Jr., 1992: Hydrographic data from Endeavor 214: A study of the Gulf Stream–Deep Western Boundary Current crossover. WHOI Tech. Rep. WHOI-92-23, 122pp.

——, W. M. Smethie Jr., J. R. N. Lazier, E. P. Jones, and W. J. Jenkins, 1996: Eddies of newly formed upper Labrador Sea Water. *J. Geophys. Res.*, **101,** 20 711–20 726.

Press, W. H., S. A. Tuekolsky, W. T. Vetterling, and B. P. Flannery, 1992: *Numerical Recipes in FORTRAN 77.* 2d ed. Cambridge University Press, 933 pp.

Randall, D. A., and B. A. Wielicki, 1997: Measurements, models, and hypotheses in the atmospheric sciences. *Bull. Amer. Meteor. Soc.*, **78,** 399–406.

Rhein, M., 1994: The Deep Western Boundary Current: Tracers and velocities. *Deep-Sea Res.*, (Part I), **41,** 263–281.

——, and Coauthors 2000: Labrador Sea Water: Pathways, CFC-inventory, and formation rates. *J. Phys. Oceanogr.*, submitted.

Sarmiento, J. L., 1983: A tritium box model of the North Atlantic thermocline. *J. Phys. Oceanogr.*, **13,** 1269–1274.

Schmitz, W. J., 1995: On the interbasin-scale thermohaline circulation. *Rev. Geophys.*, **33,** 151–173.

Smethie, W. M., Jr., 1993: Tracing the thermohaline circulation in the western North Atlantic using chlorofluorocarbons. *Progress in Oceanography,* Vol. 31, Pergamon, 51–99.

——, and R. A. Fine, 2001: Rates of North Atlantic Deep Water formation calculated from chlorofluorocarbon inventories. *Deep-Sea Res.* (Part I), **48,** 189–215.

Speer, K., and E. Tziperman, 1992: Rates of water mass formation in the North Atlantic ocean. *J. Phys. Oceanogr.*, **22,** 93–104.

Walker, S. J., R. F. Weiss, and P. K. Salameh, 2000: Reconstructed histories of the annual mean atmospheric mole fractions for the halocarbons CFC-11, CFC-12, CFC-113 and carbon tetrachloride. *J. Geophys. Res.*, **105** (C6), 14 285–14 296.

Wanninkhof, R., 1992: Relationship between wind speed and gas exchange over the ocean. *J. Geophys. Res.*, **97,** 7373–7382.

Warner, M. J., and R. F. Weiss, 1985: Solubilities of CFCs 11 and 12 in water and seawater. *Deep Sea Res.* (Part I), **32,** 1485–1497.

Watson, A. J., R. C. Upstill-Goddard, and P. S. Liss, 1991: Air–sea gas exchange in rough and stormy seas measured by a dual-tracer technique. *Nature,* **349,** 145–147.

Weiss, R. F., J. L. Bullister, F. A. Van Woy, M. J. Warner, P. K. Salemeh, and R. H. Gammon, 1991: Transient tracers in the

ocean, tropical Atlantic study: Chlorofluorocarbon measurements. Ref. Publ. 91-1, Scripps Institution of Oceanography, University of California, San Diego, La Jolla, CA, 159 pp.

WOCE Data Products Committee 1998: *WOCE Global Data, version 1.0.* WOCE Rep. 158/90, Southampton, United Kingdom, CD-ROM. [Available from U.S. National Oceanographic Data Center, 1315 East–West Highway, SSMC3, 4th Floor, Silver Spring, MD 20910.]

Wunsch, C., 1996: *The Ocean Circulation Inverse Problem.* Cambridge University Press, 442 pp.